HHS Public Access

Author manuscript

Nat Chem Biol. Author manuscript; available in PMC 2022 October 28.

Published in final edited form as:

Nat Chem Biol. 2022 August ; 18(8): 812–820. doi:10.1038/s41589-022-01015-5.

Target deconvolution of HDAC pharmacopoeia reveals MBLAC2 as common off-target

Severin Lechner[1], **Martin Ian P. Malgapo**[2], **Christian Grätz**[3], **Raphael R. Steimbach**[4,5], **Agnes Baron**[1], **Patrick Rüther**[1], **Simon Nadal**[1], **Carmen Stumpf**[1], **Christina Loos**[1], **Xin Ku**[1], **Polina Prokofeva**[1], **Ludwig Lautenbacher**[6], **Tino Heimburg**[7], **Vivian Würf**[8], **Chen Meng**[9], **Mathias Wilhelm**[6], **Wolfgang Sippl**[7], **Karin Kleigrewe**[9], **Josch K. Pauling**[8], **Karl Kramer**[1], **Aubry K. Miller**[4,10], **Michael W. Pfaffl**[5], **Maurine E. Linder**[2], **Bernhard Kuster**[1,9], **Guillaume Médard**[1]

[1)]Chair of Proteomics and Bioanalytics, TUM School of Life Sciences, Technical University of Munich, Freising, Germany

[2)]Department of Molecular Medicine, College of Veterinary Medicine, Cornell University, Ithaca, New York, USA

[3)]Animal Physiology and Immunology, TUM School of Life Sciences, Technical University of Munich, Freising, Germany

[4)]Cancer Drug Development, German Cancer Research Center (DKFZ), Heidelberg, Germany

[5)]Biosciences Faculty, Heidelberg University, Heidelberg, Germany

[6)]Computational Mass Spectrometry, TUM School of Life Sciences, Technical University of Munich, Freising, Germany

[7)]Institute of Pharmacy, Martin Luther University of Halle-Wittenberg, Halle/Saale, Germany

[8)]LipiTUM, Chair of Experimental Bioinformatics, TUM School of Life Sciences, Technical University of Munich, Freising, Germany

[9)]Bavarian Center for Biomolecular Mass Spectrometry (BayBioMS), Technical University of Munich, Freising, Germany

[10)]German Cancer Consortium (DKTK), Heidelberg, Germany

corresponding author: Guillaume Médard g.medard@tum.de.

Authors Contributions

G.M. conceived and directed the project. S.L., B.K. and G.M. wrote the manuscript. S.L. profiled the drugs, and performed the knockdown, western blots, EV purification, proteomics and lipidomics experiments. S.L. and B.K. measured the proteomics samples. M.I.P. and M.E.L. performed the MBLAC2 enzyme activity assays and C12 ceramidase assay. C.G. and M.W.P. performed the vesicle tracking experiments. R.S. and A.K.M. performed the HDAC enzyme activity assays, FRET and nanoBRET binding assays. A.B., P.R., S.N., C.S., X.K., P.P., T.H., W.S. and G.M. performed the synthetic chemistry work. S.L, A.B., P.R., S.N., C.S., C.L., X.K and P.P. performed the affinity matrices evaluation experiments. L.L. and M.W. made the data available in proteomicsDB.org. K.Kl. measured the lipidomics samples. S.L., V.W., C.M., K.Kl. and J.K.P analysed the lipidomics data. K.Kr. performed the cell imaging experiments.

Competing Interests Statement

M.W. and B.K. are cofounders and shareholders of OmicScouts and msAId. They have no operational role in either company. The remaining authors declare no competing interests.

Abstract

Histone deacetylase (HDAC) targeting drugs have entered the pharmacopoeia in the 2000s. However, some enigmatic phenotypes suggest off-target engagement. Here, we developed a quantitative chemical proteomics assay using immobilized HDAC inhibitors and mass spectrometry that we deployed to establish the target landscape of 53 drugs. The assay covers 9 of the 11 human zinc-dependent HDACs, questions the reported selectivity of some widely-used molecules, notably for HDAC6, and delineates how the composition of HDAC complexes influences drug potency. Unexpectedly, metallo-beta-lactamase domain-containing protein 2 (MBLAC2) featured as a frequent off-target of hydroxamate drugs. This poorly characterized palmitoyl-CoA hydrolase is inhibited by 24 HDAC inhibitors at low nM potency. MBLAC2 enzymatic inhibition and knock down led to the accumulation of extracellular vesicles. Given the importance of extracellular vesicle biology in neurological diseases and cancer, this HDAC-independent drug effect may qualify MBLAC2 as a target for drug discovery.

Main

Inhibition of histone deacetylases (HDACs) has emerged as a promising therapeutic option in oncology as well as further conditions such as Duchenne Muscular Dystrophy[1]. The FDA-approval of the first-in-class HDAC inhibitor (HDACi) Vorinostat in 2006 for the treatment of cutaneous T-cell lymphoma marked the start of a series of drug approvals for cancerous diseases. Notably, most clinical HDACis engage several targets across the four classes of human zinc-dependent HDACs (I, IIa, IIb, and IV). Such pan-HDACis and their polypharmacological mechanisms of action (MoA) might be beneficial particularly in oncology, where multiple disease-relevant class I and II HDACs are inhibited simultaneously[2]. However, conditions such as Amyotrophic Lateral Sclerosis or Huntington's Disease would require class II isoform-selective inhibitors that precisely interfere with the pathologic mechanism[3, 4] but bypass the toxicity arising from inhibition of epigenetic class I HDACs[2]. Therefore, the delineation of the target spectrum of HDACis appears essential for the understanding of their MoAs and for the development of more bespoke therapies.

HDAC activity highly depends on molecular context such as post-translational modifications (PTMs)[5], allosteric factors[6] or participation in gene regulatory protein complexes[7]. These factors have been shown to impact drug affinity but are not recapitulated in traditional enzyme activity assays[8, 9]. To address this challenge, a landmark study[8] reported a chemoproteomic assay that probes HDACi target engagement in lysates containing natively folded proteins, their cofactors and maintaining biomolecular interactions. The immobilization of Vorinostat allowed for the pulldown of HDAC complexes and competitive drug binding enabled the selectivity profiling of 16 HDACis against 6 of the 11, more particularly class I and IIb, HDACs. These chemoproteomic experiments led to the discovery of the Mitotic Deacetylase Complex (MiDAC), which was later shown to be relevant for correct mitotic chromosome alignment[10]. Moreover, the study revealed that aminoanilide-based HDACis exhibit reduced affinity for the Sin3 HDAC-complex and slow binding kinetics[8, 9]. So far, however, affinity matrices designed to profile HDAC drugs do not address class IIa HDACs[11], which are targets of rising interest[12].

Here, we substantially extended the existing profiling technology by creating an affinity matrix able to enrich 9 of 11 Zn^{2+}-dependent HDACs (Zn-HDACs), now including class IIa, and mapped the target landscape of 53 HDAC and metallohydrolase drugs. The results highlight HDACis with unexpected target profiles and low selectivity. However, we also identify drugs with unparalleled selectivity for class IIb HDAC6 and HDAC10. Moreover, the quantitative data revealed that drugs interacting with HDAC1 as part of gene regulatory CoREST complexes[13] containing either RCOR1 or RCOR3 show a larger than ten-fold difference in HDAC1 binding affinity. Surprisingly, about half of the HDACis, including clinically advanced molecules, inhibit the acyl-CoA hydrolase metallo-beta-lactamase domain-containing protein 2 (MBLAC2)[14] at nano-molar concentrations. We further demonstrate that pharmacological inhibition or knockdown of MBLAC2 triggers accumulation of extracellular vesicles in cell culture, placing this poorly characterized protein into the context of extracellular vesicle biology.

Results

Optimized chemoproteomics assay for HDAC drugs profiling.

Inspired by previous chemoproteomic studies of HDAC drugs[11], we embarked on the development of a general affinity matrix to enrich the HDAC protein family comprehensively. Therefore, we synthesized 15 chemical probes (**1** – **15**) (Extended Data Fig. 1a) representing different chemotypes, including different zinc-binding groups, and immobilized them on beads. We then evaluated the obtained affinity matrices for their suitability in pulling down HDACs from lysates of ten cell lines with different HDAC expression profiles, akin to the Kinobeads or other similar chemical proteomics approaches[15]. This led to the identification of a combination of three probes (iC, iQ and iA) and lysates of two cell lines (MV4–11 and SW620) that, together, covered the widest range of targets (Fig. 1a, Extended Data Fig. 1 and 2). Specifically, iC robustly enriched seven HDACs including class IIa HDAC4,5 and 7 as well as MBLAC2). Addition of iQ improved the enrichment of HDAC3 and HDAC8, extending the coverage of the affinity matrix to 9 of the 11 Zn-HDACs. We also included iA, since we observed that it enriched many metalloenzymes, including iron-sulfur cluster proteins (Extended Data Fig. 2, Fig. 1a) as well as GATD3A, ALDH2, ISOC1, and ISOC2 that turned out to be common HDACi off-targets (see below).

With this broad affinity matrix in hand, the target profiles of drugs can be obtained by competition experiments. Here, the drug of interest is added in increasing doses to the lysate in which it engages its targets and, thereby, prevents specific binding of the same targets to the matrix in a dose-dependent fashion (Supplementary Fig. 1)[8]. Plotting the relative intensities of matrix-binding proteins over increasing doses of free drug allows derivation of EC_{50} and apparent K_d values (K_d^{app}) that characterize the interaction (see methods). Importantly, binding equilibrium between the molecule and the targets is essential to obtain meaningful K_d^{app} values. To account for the slow on-rates of the aminoanilide-based inhibitors[9, 16], we evaluated incubation temperatures of 4 °C and 22 °C (hereafter: room temperature, RT) for two representative HDACis set to compete at 30 μM over a time course of up to 25 h. At 4 °C, the hydroxamate inhibitor CHDI00465983 engaged with

class IIa HDACs within a few minutes, while the aminoanilide Entinostat only maximally competed target HDACs after more than 2 h. This reflects the already reported differences in binding kinetics of hydroxamates and aminoanilides, the latter featuring extremely slow k_{on} rates[9]. Increasing incubation temperature, however, significantly accelerated reaching binding equilibrium for the aminoanilide Entinostat (Fig. 1b, Extended Data Fig. 3). We then validated a protocol with a 90 min total incubation time (60 min drug pre-incubation and 30 min pulldown) at 30 °C that could accommodate for very slow binders. Here, we profiled Trichostatin A, Mocetinostat, Vorinostat, Romidepsin, and Panobinostat and compared the results to previously published HDACi profiling studies[8, 16, 17]. In general, our data agrees well with compared literature values. For instance, dose responses of Romidepsin showed competition of HDACs from class I, IIb and IIa (Fig. 1c) and pK_d^{app} values correlated well ($R^2 = 0.89$) with enzyme activity assays[17] (Fig. 1d) and were consistent with BRET-based in-cell target engagement data[16] (Extended Data Fig. 4). We found lower correlation with an initial chemoproteomics study[8]. In particular, the slow binder Mocetinostat showed higher affinities here than originally published[8]. However, the authors have acknowledged their initial affinity underestimation of aminoanilides in a later study, where they optimized the incubation conditions[9]. Remarkably, K_d^{app}s for Panobinostat correlated extremely well ($R^2 = 0.92$) to a more recent study using immobilised Panobinostat (Fig. 1e)[18]. These experiments validate the approach and extend the assayed target spectrum over published data sets.

The target landscape of HDAC drugs.

We next profiled 53 molecules comprising the majority of all clinical HDAC drugs, several HDAC tool compounds and five hydroxamate-based metallohydrolase drugs (see Supplementary Fig. 2 for structures). Only a few vignettes of the data can be highlighted in this manuscript but the complete profiling data can be dynamically explored via ProteomicsDB (https://www.proteomicsdb.org/)[19]. Neither the HDAC activity modulator Tasquinimod nor the five metallohydrolase inhibitors (Batimastat, Ilomastat, Prinomastat, Marimastat, and Salicylhydroxamic acid) bound HDACs or other metalloproteins with K_d^{app} values below 30 μM. Somewhat surprisingly, the same was observed for the four HDACis Resminostat, BRD73954, HPOB, and TH147. Expectedly, Valproic acid and Phenylbutanoic acid displayed weak (three-digit micromolar) affinities (Supplementary Data 1). Clustering of the remaining 41 HDACis that have at least one micromolar target protein, organized the compounds into four major groups (Fig. 2a). Group A comprises the aminoanilides that are selective for binding HDAC1/2/3 only. Group B comprises the thiolate Romidepsin and hydroxamic acid-based pan-HDACis that often also engage MBLAC2. Interestingly, the most potent pan-HDAC inhibitors Quisinostat and Romidepsin differ in the one class IIb HDAC they engage. While Romidepsin binds HDAC6 with high affinity, Quisinostat potently binds HDAC10 but not HDAC6, constituting an exception amongst the hydroxamic acid inhibitors. The peptidic capping group of the natural compound Romidepsin does not closely mimic the non-peptidic polyamine substrates of HDAC10 which might explain its poor affinity for HDAC10. Group C features rather unselective HDACis (including approved and clinical drugs such as Vorinostat) that also bind non-HDAC off-targets, notably ALDH2 and the uncharacterized proteins ISOC1, ISOC2, and GATD3A. Group D, in contrast to groups A-C, is characterized by drugs that do not engage HDAC1/2/3. This group includes

the most selective and potent class IIa inhibitors CHDI00390576 and CHDI00465983 which primarily target HDAC5 and HDAC7 as well as TMP195, with preferred binding for HDAC7 over HDAC4 and HDAC5. Live-cell imaging of drug treated (at 100 nM and 1 μM) SW620 colorectal cancer cells highlighted the most potent HDAC1/2/3 inhibitors of groups A-C to impact cell vitality, while group D drugs did not induce an altered cell morphology (Extended Data Fig. 5). Exploring this landscape from a target perspective, 29 compounds (>50% of the total) bound class I HDACs, reflecting the efforts expended in developing therapeutic modulators of these targets and 26 molecules bound class IIb HDACs. In contrast, only six drugs targeted class IIa HDACs. Interestingly, MC1568 and LMK235, which are frequently used as class IIa-specific probes, showed no class IIa target engagement at all in our assay, questioning their use as chemical probes but rationalising the poor HDAC enrichment by probes based on these molecules (Fig. 2 and Extended Data Fig. 1e).

Selectivity of HDAC inhibitors.

The chemical proteomics data assembled here provided an opportunity to assess the selectivity of the HDACis for their targets. As a metric, we used the concentration- and target-dependent selectivity (CATDS) score[20] which is based on measuring the extent of target engagement by a drug. Target engagement refers to the fraction of all protein molecules that are bound by the drug at a particular drug concentration. By that definition, CATDS compares the half maximal target engagement of a particular drug to a target of interest (i.e. the relative residual binding value of 0.5 for the pK_d^{app} of that drug:target interaction) to the sum of target engagements of all targets at that same drug concentration (see methods and Supplementary Fig. 3). Systematic CATDS calculation for all drugs and targets confirmed PCI-34051 as the only selective HDAC8 inhibitor[21] (Fig. 2b, Supplementary Table 1). Interestingly, we found the HDAC6 inhibitor Tubastatin A to be the second most selective HDAC10 inhibitor (CATDS = 0.67). This finding contrasts the original and recent reports[22] (Fig. 2c) but agrees well with published in-cell nano-BRET binding assays[23]. Furthermore, the pan-HDAC inhibitor Abexinostat had the highest HDAC10 affinity in the panel of drugs ($pK_d^{app\ HDAC10}$ = 7.8 vs. $pK_d^{app\ HDAC1}$ = 6.1) in sharp contrast to the original report (pK_i^{HDAC10} = 7.6 vs. pK_i^{HDAC1} = 8.2)[24]. Surprisingly, our analysis revealed TH65 as a selective inhibitor for HDAC10 (CATDS = 0.83, pK_d^{app} = 6.2) (Fig. 2c). TH65 was designed as an inhibitor of *schistosoma mansoni* HDAC8 but not tested for human HDAC10 inhibition[25]. According to ChemicalProbes.org, no highly selective HDAC10 probes have been reported yet but our data designates TH65 as novel promising chemical probe for HDAC10 with at least 30-fold selectivity (limit of our assay) over other HDACs. We profiled selected HDAC inhibitors in biochemical enzyme assays and confirmed the selectivity of TH65: TH65 inhibited HDAC10 binding with EC50 values comparable to Vorinostat and Ricolinostat in a FRET assay, but had the lowest activity against HDAC1/2/3/6 of the panel of drugs and, like Vorinostat, very low activity against HDAC8 (Extended Data Fig. 6a, Supplementary Table 2). We then demonstrated in-cell target engagement of TH65 by nano-BRET assays for HDAC10 and HDAC6 catalytic domain 2 (CD2). In this assay, the affinity of TH65 for HDAC10 was about 5-fold higher than for HDAC6 (Extended Data Fig. 6b, Supplementary Table 2).

Focussing on the second member of class IIb, our data questions the purported selectivity of HDAC6 probes such as Tubacin, Nexturastat A, Tubastatin A and others (Fig. 2d). For instance, Nexturastat A showed no substantial difference in affinity between HDAC6 and HDAC10 ($pK_d^{app\ HDAC6}$ = 6.4 vs. $pK_d^{app\ HDAC10}$ = 6.0), contrasting reported values (pEC_{50}^{HDAC6} = 8.3 vs. pEC_{50}^{HDAC10} = 5.1)[26], but in line with recently reported nano-BRET data[23]. Furthermore, Nexturastat A also potently engages MBLAC2 (pK_d^{app} = 7.6), a novel finding that reduces the drugs' apparent selectivity. Intriguingly, the two clinical designated HDAC6 inhibitors Ricolinostat and Citarinostat showed only slightly preferred binding for HDAC6 over class I HDACs, resulting in poor selectivity scores (Fig. 2d). Among all HDAC6-binding molecules, ACY-738 was the only compound with a perfect CATDS score of 1 (Fig. 2d). The selectivity of its close analogue ACY-775 was lower (CATDS = 0.52) owing to the nearly equipotent binding of MBLAC2. We confirmed the selectivity of ACY-738 in biochemical activity assays and its cellular target engagement in nano-BRET assays (Extended Data Fig. 6a-d, Supplementary Table 2). Considering the exquisite selectivity and its submicromolar affinity, ACY-738 currently appears to be the chemical probe of choice for HDAC6.

HDACi affinity depends on the composition of HDAC complexes.

HDACs 1–3 exert their functions as part of protein complexes and, when tight complexes are formed, endogenous HDAC interactors are also captured by the affinity matrix. In the competition assay, complex partners are competed together with their interacting HDAC and therefore also show dose-response curves that allow to infer the affinity of drugs to HDACs in complex with their respective interactors (Extended Data Fig. 7a). This allowed us to interrogate the binding of HDACis to five HDAC complexes systematically, using the acquired data. The CoREST, NuRD, Sin3 and MiDAC complex are formed around a core of 1–2 isoforms of HDAC1 or HDAC2, while the NCoR complex is formed around HDAC3[13]. In accordance to published results[8, 9], we did not observe a general difference between drug chemotypes with respect to preferential binding to HDAC3 when part of the NCoR complex or to HDAC3 in isolation (Extended Data Fig. 7b). Regarding HDAC1 and HDAC2-containing complexes, however, we observed an impact of the HDAC interactome on drug affinity. For instance, Trichostatin A showed a 14-fold EC_{50} difference (ΔpEC_{50}) between HDAC1 when part of the MiDAC complex (illustrated by its member DNTTIP1) compared to HDAC1 that is not part of the complex (Fig. 3a). Even more strikingly, RCOR3 showed an >10-fold lower EC_{50} value compared to RCOR1 and other CoREST members, which was observed most prominently for Panobinostat, Romidepsin, Dacinostat and M344 (Fig. 3b). These measurements support the existence of drug selectivity between variants of the same complex depending on its (mutually exclusive) subunits. To generalize the above, we calculated ΔpEC_{50} for HDAC1 and each complex protein (Fig. 3c). This led to a clear distinction between aminoanilides and the other drugs. Aminoanilides showed decreased potency for HDAC1/2 when part of complexes (ΔpEC_{50} coloured in red) while hydroxamates showed generally increased potency (ΔpEC_{50} coloured in blue). Enhanced affinity to RCOR3-interacting HDACs was observed for the majority of hydroxamic acid inhibitors. These data confirm and extend previous observations that HDACi target engagement strongly depends on the composition of HDAC complexes and thus provides prospects for the development of further HDAC complex-specific drugs.

Acyl-CoA hydrolase MBLAC2 is a common off-target of HDACis.

The perhaps most unexpected result of this study was the observation of MBLAC2 as an off-target of 24 hydroxamate molecules (Fig. 2a). Amongst those are approved drugs such as Panobinostat (pK_d^{app} = 5.9) and frequently used tool compounds such as Nexturastat A (pK_d^{app}= 7.6) (Fig. 4a). To ascertain that inhibition of binding equals inhibition of enzymatic activity, we deployed a recombinant enzyme activity assay that measures the MBLAC2-catalyzed hydrolysis of ^{3}H-labeled palmitoyl-CoA (Fig. 4b)[14]. MBLAC2 activity was affected by nearly all binders at 300 nM drug concentration and reduced to background for 18 HDACis (Fig. 4c). HDAC drugs (e.g. Tucidinostat, PCI-34051) that showed no or very weak MBLAC2 binding in the chemoproteomic assay had little if any effect on enzyme activity. Full dose-response assays for 11 compounds determined that most hit the experimental EC_{50} limit of 5–10 nM (i.e. pEC_{50} of ca. 8.0–8.3), which corresponds to 50% of the applied enzyme concentration. Notably, these potent inhibitors included the approved drug Panobinostat (pEC_{50} > 8.0) and the orphan drug Pracinostat (pEC_{50} > 8.2) (Fig. 4d, Extended Data Fig. 8). In contrast, the approved aminoanilide Tucidinostat did not affect MBLAC2 activity even at a 1,000-fold higher concentration. Also in concordance with the competition binding data, ACY-775 is a very potent MBLAC2 inhibitor (pK_d^{app} = 6.1, pEC_{50} > 8.2), while the chemically closely related compound ACY-738 is >75-fold less potent ((pK_d^{app} < 4.5, pEC_{50} = 6.3; Fig. 4e).

MBLAC2 inhibition leads to EV accumulation.

MBLAC2 is a poorly characterized protein. Yet, it has been shown to interact with the palmitoyltransferase ZDHHC20[14], a regulator of endocytosis-mediated EGFR internalization[27], as well as other proteins whose GO term enrichment hints at roles in endo- or exocytosis (BioPlex, Supplementary Data 2)[28]. Concurring GO annotations were also found when analysing the localisation and roles of MBLAC2-coregulated proteins (proteomeHD)[29] (Supplementary Data 2). In addition, the HDAC6 inhibitor Tubacin has been shown to produce a strong vesicle phenotype that cannot be attributed to HDAC6 inhibition[30]. Since we identified Tubacin to inhibit MBLAC2 (Fig. 2a, 4c), we speculated that the vesicle phenotype may be related to MBLAC2 activity. Knocking down (KD) >85% of the protein in HEK293 cells using siRNA did not have a substantial effect on the expression of 7,112 monitored proteins including those known to be associated with MBLAC2 and vesicle biology (Extended Data Fig. 9a,b, Supplementary Data 3). However, the knockdown indeed induced accumulation of extracellular vesicles in the cell culture supernatants (Fig. 5a). This accumulation was even more pronounced upon pharmacological inhibition of MBLAC2 by ACY-775 (Fig. 5b), compared to treatment with its close analogue ACY-738 (Fig. 2a). ACY-738 and ACY-775 inhibit HDAC6 with similar potency in the chemoproteomic assay (ACY-775 pK_d^{app} = 6.4 vs. ACY-738 pK_d^{app} = 6.7), and comparable effect on acetylation of HDAC6 substrate alpha-tubulin is also observed (Extended Data Fig. 10). In contrast, only ACY-775 is a potent MBLAC2 binder and inhibitor (pK_d^{app} = 6.1, pEC_{50} = 8.2), while ACY-738 is not (pK_d^{app} <4.5, pEC_{50} = 6.3). Together, these data suggest a role of MBLAC2 activity in extracellular vesicle levels.

Considering the involvement of lipids and particularly ceramides in vesicle budding[31], we tested if MBLAC2 inhibition has an effect on the lipid composition of the cell. Untargeted

mass spectrometry-based lipidomics following MBLAC2 knock-down revealed changes in the levels of several lipids. For instance, hexosylceramides were significantly downregulated but sphingomyelins were generally upregulated (Fig. 5c, Extended Data Fig. 9c, and Supplementary Data 4). While we could not demonstrate ceramidase activity of MBLAC2 using a fluorescently labelled C12-ceramide model substrate (Extended Data Fig. 9d-g), the observed changes in lipid composition may still be the direct or indirect result of inhibiting one or several MBLAC2 activities and may provide a link to the well-studied effects of ceramides in vesicle biogenesis pathways[31].

Discussion

The current study makes several noteworthy contributions to the field of chemical biology. The profiling data for the 53 drugs targeting HDACs and metallohydrolases is the most comprehensive to date and constitutes a rich resource for chemical biologists and medicinal chemists. The collective data enabled several analyses not possible in small data sets and revealed a number of surprises.

First, the novel affinity matrix goes beyond the state of the art[8, 11, 18, 32] as it enriches 9 out of the 11 human zinc-dependent HDACs including class IIa HDACs. This improvement mostly stems from the development of iC, featuring a diarylcyclopropane-hydroxamic acid chemotype developed for HDAC5 inhibition[33, 34]. In this series of inhibitors, enantiomerically pure CHDI00465983 is class IIa selective (Fig. 2), while iC (composed of three enantiomer pairs) exhibits pan-HDAC as well as off-target MBLAC2 binding characteristics. Immobilised Quisinostat, iQ, enriches HDAC8 better than immobilized Vorinostat (**6**) or any other affinity matrix tested. Off-targets GATD3A, ALDH2, ISOC1, and ISOC2 could only be identified because of their robust enrichment by iA. We note that the sterically permissive alkyl chain of iA, also found in all HDACis constituting group B (Fig. 2a, Supplementary Fig. 2), might also favourably position the metal-binding hydroxamate in the active sites of many other metalloproteins leading to their enrichment (Extended Data Fig. 2). Further work aims at identifying HDAC9- and HDAC11-rich cell lines and a dedicated HDAC11 probe. As it stands, the affinity matrix may also be leveraged to investigate HDACi repurposing against e.g. parasites such as *Schistosoma Mansoni* or *Plasmodium Falciparum*[35], owing to the particularly high HDAC preservation across the species phylogeny.

Second, it is obviously important to know which proteins are engaged by a given drug, how potent the drug is for that target and what its selectivity is over other targets to be able to attribute an observed biological effect to the target(s) of the compound. For example, for the designated HDAC6 inhibitors Ricolinostat ($pK_d^{app\ HDAC6}$ = 7.1) and Citarinostat ($pK_d^{app\ HDAC6}$ = 6.7), the narrow selectivity window is consistent with an earlier study attributing their main anti-cancer effects to HDACs 1–3 inhibition (pK_d^{app} range of 4.9–6.0, Fig. 2) rather than HDAC6[36]. More surprisingly, Tubastatin A has been used in >100 publications to probe HDAC6 biology under the assumption of high HDAC6 selectivity[22]. According to our results, however, Tubastatin A has a much higher potency for HDAC10 than HDAC6 ($pK_d^{app\ HDAC10}$ = 7.5 vs. $pK_d^{app\ HDAC6}$ = 5.0). We hypothesize that the discrepancy between the published HDAC activity inhibition data and the chemoproteomic

binding data as well as in-cell target engagement data (nanoBRET[23]), originate from the inadequacy of the peptidic substrate used in earlier studies: HDAC10 was only recently annotated as a polyamine rather than protein deacylase[37]. In this regard, the most potent HDAC10 binders in our assay (Tubastatin A, Abexinostat, Pracinostat, Quisinostat, Panobinostat, Dacinostat) all feature a positively charged amino group reminiscent of the charged polyamine substrate that interacts with the gatekeeper glutamate (Glu272 or potentially Glu22) of HDAC10[23]. High selectivity is however achievable. Three drugs even fulfil prime criteria for a chemical probe (sub-micromolar potency, 30-fold window over other targets)[38]: ACY-738 for HDAC6, PCI-34051 for HDAC8 and TH65 for HDAC10. Their identification will serve chemical biology, as, for instance, TH65 could probe the roles of HDAC10 in polyamine biology and autophagy as well as neuroblastoma[23, 37, 39, 40].

Third, it is evident from the target landscape, that the design of inhibitors that discriminate between the very similar active sites of HDAC1,2 and HDAC3 is challenging. Selectivity may here be obtained with drugs that target particular HDAC complexes[13], such as CoREST-selective HDACi to treat synaptopathies[41]. Chemoproteomic profiling preserves HDAC complexes which led to the observation that hydroxamic acid drugs tend to prefer binding to CoREST, Sin3 and MiDAC complexes (Fig. 3c). Surprisingly, some of those drugs bind with >10-fold higher affinity to HDAC1 or HDAC2 when interacting with RCOR3 instead of the alternative CoREST subunit RCOR1. In contrast to hydroxamates, aminoanilide drugs appear to bind better to HDACs that are not part of a complex. This agrees with a recent report about aminoanilide drugs engaging free HDACs and staying entrapped in the active site after formation of a complex with rigidified HDAC dynamics[42]. The data suggests that different classes of HDAC drugs (hydroxamates versus aminoanilides) might differentially modulate the acetylation of HDAC substrates according to their preference for one of the complexes or the HDACs in isolation.

Fourth, chemoproteomic profiling is set to identify unexpected targets for otherwise well characterized drugs. For instance, we and others have identified novel targets of kinase inhibitors within (e.g. activin receptor ALK2 for the ATM inhibitor CP466722)[43] or outside the target class (e. g. ferrochelatase for the BRAF inhibitor Vemurafenib)[44]. The current study uncovered five such cases for HDAC inhibitors, notably ALDH2 (n=9 drugs, most potent pK_d^{app} = 6.5), GATD3A (n=7 drugs, most potent pK_d^{app} = 5.8), ISOC1 (n=7 drugs, most potent pK_d^{app} = 6.8), ISOC2 (n=8 drugs, most potent pK_d^{app} = 8.2) and MBLAC2 (n=24 drugs, most potent pK_d^{app} = 7.6). Interestingly, MBLAC2 was bound by several HDACi groups. The other off-targets seem to be preferentially bound by HDACis whose hydroxamic acid is presented via an alkyl chain. Hence, the alkyl may favour off-target binding while HDACis with conjugated or aromatic linkers will be more selective for HDACs. All off-targets but ALDH2 are poorly characterized proteins and it remains to be investigated whether HDACi binding affects their biological function and thus impacts drug efficacy. Intriguingly, ISOC1 knockdown has been reported to inhibit cancer cell proliferation and metastasis[45], which may be a desirable off-target effect of e. g. Vorinostat. Droxinostat and Bufexamac did not bind HDACs in our assay but their affinity for some of the off-targets may be used to probe the function of these proteins.

Fifth, among the non-HDAC off-targets, MBLAC2 stands out for its potent and frequent binding to hydroxamic acid HDAC inhibitors. This protein has recently been shown to hydrolyse acyl-CoA and, just like HDACs, utilizes Zn^{2+} for catalysis[14]. Our data show, for the first time, that HDACis can inhibit the palmitoyl-CoA hydrolase activity of the enzyme *in vitro* and several do so with single digit nano-molar EC_{50}. Interestingly, a study describing an HDAC6-independent stimulatory effect of Tubacin on exosome biogenesis[30] led us to hypothesise that this phenotype may stem from the inhibition of MBLAC2, the only off-target of Tubacin in our chemoproteomic assay. Given that MBLAC2 can hydrolyze palmitoyl-CoA, the initial building block of ceramides, we speculated that MBLAC2 might be involved in regulating ceramide levels and exosome release. In line with such a putative role, treatment with the dual MBLAC2/HDAC6 inhibitor ACY-775 led to accumulation of extracellular vesicles compared to treatment with the HDAC6 selective ACY-738. This finding suggests a direct or indirect role of MBLAC2 in extracellular vesicle biology, which we substantiated by MBLAC2 knockdown experiments. Importantly, differential effects of ACY-775 and ACY-738 have been observed before, such as a more pronounced activity on mitochondria number and axonal transport for ACY-775 compared to ACY-738 in a genetic mouse model of Charcot-Marie-Tooth disease[46]. Interestingly, other inhibitors we found to be dual MBLAC2/HDAC6 inhibitors are investigated in neurological diseases, for instance to improve axonal transport of brain-derived neurotrophic factor (BDNF) vesicles and BDNF release[47, 48]. It is therefore tempting to hypothesise a synergy between effects on extracellular vesicle level via MBLAC2 inhibition and HDAC6-linked effects on microtubular vesicle transport and fusion[49]. We then started to explore which molecular events in the lipidome connect MBLAC2 inhibition and extracellular vesicle accumulation. While we could not evidence MBLAC2 C12-ceramidase activity as potential regulatory mode of vesicle budding[31], MBLAC2 might hydrolyze other lipids in cells. Such a lipidase activity has indeed been elucidated for at least one of the 18 human metallo-beta-lactamase domain containing proteins, i.e. N-acyl-phosphatidylethanolamine-hydrolyzing phospholipase D (NAPEPLD)[50]. In fact, MBLAC2 knockdown had an effect on intracellular concentrations of some lipid families, including a general decrease of hexosylceramides and a concomitant increase of sphingomyelin levels. We anticipate that the identified MBLAC2 inhibitors will inspire biologists to further probe MBLAC2 cellular functions and help understand its connection to extracellular vesicle accumulation.

To conclude, this study has shown how the design and synthesis of promiscuous affinity probes enabled the delineation of the target landscape of HDACis. The drug profiles, assembled in the freely accessible online database ProteomicsDB, inform medicinal chemistry and highlight chemical probes to study biology. The surprising identification of MBLAC2 as an HDACi target helped placing this poorly characterized protein into a functional context and may provide the basis for future drug discovery programs focussed on vesicle pathobiology.

Methods

Preparation of iC (1).

4-Azidobutanamine (1 μmol) was reacted with DMSO-washed NHS-activated (~20 μmol/mL beads) sepharose beads (1 mL) and triethylamine (20 μL) in DMSO (2 mL) on an end-over-end shaker overnight at RT in the dark. Aminoethanol (50 μL) was then added to inactivate the remaining NHS-activated carboxylic acid groups. After 1 h the beads were washed with 40 mL DMSO.

Alkyne-NHOTHP (**19**) (1 μmol) (Supplementary Note) was then clicked to the azide-functionalised beads via incubation in 1:1:2 (v/v/v) DMSO:tBuOH:H_2O (2 ml total volume including beads), 0.1 mM TBTA, 2 mM $CuSO_4$ and 2 mM sodium ascorbate for 16h at RT in the dark on the end-over-end shaker. The beads were then washed with 20 mL of 1:1:2 (v/v/v) DMSO:tBuOH:H_2O, 30 mL of 50 mM EDTA in water and 30 mL ethanol, then reacted with 10 mM HCl inEtOH (10 mL) for 16h at RT in the dark. Beads were washed with 50 mL ethanol to yield **iC**, stored at 4 °C in EtOH.

Preparation of iQ (5).

Quisinostat (1 μmol) was reacted with DMSO-washed NHS-activated (~20 μmol/mL beads) sepharose beads (1 mL) and triethylamine (20 μL) in DMSO (2 mL) on an end-over-end shaker overnight at RT in the dark. Aminoethanol (50 μL) was then added to inactivate the remaining NHS-activated carboxylic acid groups. After 16 hours the beads were washed with 10 mL DMSO and 30 mL EtOH to yield **iQ**, stored at 4 °C in EtOH.

Preparation of iA (7).

6-Aminocaproic acid (1 μmol, 100 μL of 10 mM stock solution in 50 mM HCl tBuOH) was reacted with DMSO-washed NHS-activated (~20 μmol/mL beads) sepharose beads (1 mL) and triethylamine (15 μL) in DMSO (2 mL) on an end-over-end shaker for 16 h at RT in the dark. (TLC with Kaiser test staining was used to monitor successful conversion). Aminoethanol (50 μL) was then added to inactivate the remaining NHS-activated carboxylic acid groups. After 2 h on an end-over-end shaker at RT, the beads were washed with DMSO (4 × 10 mL) and resuspended in anhydrous DMF (2 mL total volume). HATU (10 μmol, 100 μL of 100 mM stock in DMF), O-(tetrahydro-2Hpyran-2yl)-hydroxylamine (12 μmol, 120 μL of 100 mM stock in DMF), Hünig's base (20 μmol, 100 μL of 200 mM stock in DMF) and triethylamine (20 μL) were then added and the beads were incubated at RT for 16 h on an end-over-end shaker. Next, the beads were washed with 10 mL DMF and 30 mL ethanol, then reacted with 10 mM HCl in EtOH (10 mL) for 16 h at RT in the dark to deprotect the hydroxamate. Beads were washed with EtOH (3 × 10 mL) to yield **iA**, stored at 4 °C in EtOH.

Preparation of other affinity matrices (2–4, 6, 8–15).

Amino-linkable compounds respectively **26, 31, 37,** commercial linkable SAHA (p-Aminomethyl Vorinostat, Toronto Research Chemicals, A617070)**, 44, 45, 52, 57, 60, 64, 66, 69** (Supplementary Note) were immobilized on DMSO-washed NHS-activated sepharose beads with a coupling density of 1 μmol per mL beads via incubation with 20

µL triethylamine per mL beads on an end-over-end shaker for 20 h at RT in the dark. Remaining free NHS-groups were inactivated by blocking with 50 µL of aminoethanol per mL beads.

Preparation of cell lysates for affinity pulldown assays.

Cell lines COLO-205, MV4–11, K-562, BT-549 and PC3 were grown in RPMI 1640 medium (PAN Biotech), SW620, OVCAR-8 and MCF7 were grown in IMDM medium (PAN Biotech), PATU-8998-S as well as SK-N-BE(2) were cultured in DMEM/HAM's F-12 medium (PAN Biotech) and HEK293 in DMEM (PAN Biotech). All media were supplemented in with 10% FBS (PAN Biotech) and cell lines were internally tested for Mycoplasma contamination. Cells were lysed in lysis buffer (0.8% Igepal, 50 mM Tris-HCl pH 7.5, 5% glycerol, 1.5 mM $MgCl_2$, 150 mM NaCl, 1 mM Na_3VO_4, 25 mM NaF, 1 mM DTT and supplemented with protease inhibitors (SigmaFast, Sigma) and phosphatase inhibitors (prepared in-house according to Phosphatase inhibitor cocktail 1, 2 and 3 from Sigma-Aldrich)). The protein amount of cell lysates was determined by Bradford assay and adjusted to a concentration of 5 mg/mL.

(Competition) Pulldown assays.

For the selectivity profiling of HDAC inhibitors, lysates from SW-620 and MV4–11 cell lines were combined in a 1:1 ratio of protein amount to give a lysate mix with 5 mg/mL protein concentration. The 0.5 mL lysate mix (adjusted to 5 mg/mL protein concentration and 0.4% Igepal) was pre-incubated with 9 doses of HDAC inhibitor (DMSO vehicle, 3 nM, 10 nM, 30 nM, 100 nM, 300 nM, 1000 nM, 3000 nM, 30000 nM or for Valproic acid and Phenylbutanoic acid DMSO, 1 µM, 3 µM, 10 µM, 30 µM, 100 µM, 300 µM, 1000 µM, 3000 µM) for 1 h at 30 °C in an end-over-end shaker, followed by incubation with 18 µL affinity matrix (1:1:1 mixture of iC, iQ and iA) for 30 min at 30 °C in an end-over-end shaker.

To assess the degree of protein depletion from lysates by the affinity matrix, a second pulldown (PDPD) with fresh beads was performed using the unbound protein fraction from the vehicle control flow through.

The beads were washed (1× 1 mL of lysis buffer without inhibitors and only 0.4% Igepal, 2× 2mL of lysis buffer without inhibitors and only 0.2% Igepal) and captured proteins were denatured with 8 M urea buffer, alkylated with 55 mM chloroacetamide and digested with Trypsin according to standard procedures. Resulting peptides were desalted on a C18 filter plate (Sep-Pak® tC18 µElution Plate, Waters), vacuum dried and stored at −20 °C until LC-MSMS measurement.

Other pulldown-based assays were performed according to the same protocol with minor changes: For triplicate pulldowns assessing cell line typical HDAC expression or affinity matrix enrichment properties, the pre-incubation step with HDAC inhibitor as well as the PDPD were omitted and pulldown was performed at 4 °C for 45 min. For Pulldown assays for probe comparison (Extended Data Fig. 1), 1 mg protein from a 1:1 mix of MV4–11 and SW620 lysate was used as input. For kinetics experiments the pre-incubation with 30 µM compound was performed over increasing time periods (0 min, 15 min, 30 min, 1 h, 2 h, 6 h,

8 h, 24 h at 4 °C and 0 min, 15 min, 30 min, 45 min, 1 h, 2 h, 4 h, 6 h, 8 h at 22 °C) followed by pulldown at 4 °C for 45 min or at 22 °C for 15 min.

LC-MSMS measurement of (competition) pulldown assays.

Peptides were analyzed via LC-MS/MS on a Dionex Ultimate3000 nano HPLC coupled to an Orbitrap HF (Thermo Fisher Scientific) mass spectrometer, run via the Thermo Scientific Xcalibur software. Peptides were loaded on a trap column (100 µm x 2 cm, packed in house with Reprosil-Gold C18 ODS-3 5 µm resin, Dr. Maisch, Ammerbuch) and washed with 5 µL/min solvent A (0.1 % formic acid in HPLC grade water) for 10 min. Peptides were then separated on an analytical column (75 µm x 40 cm, packed in house with Reprosil-Gold C18 3 µm resin, Dr. Maisch, Ammerbuch) using a 50 min gradient ranging from 4–32 % solvent B (0.1 % formic acid, 5 % DMSO in acetonitirile) in solvent A (0.1 % formic acid, 5 % DMSO in HPLC grade water) at a flow rate of 300 nL/min.

The mass spectrometer was operated in data dependent mode, automatically switching between MS1 and MS2 spectra. MS1 spectra were acquired over a mass-to-charge (m/z) range of 360–1300 m/z at a resolution of 60,000 (at m/z 200) in the Orbitrap using a maximum injection time of 10 ms and an automatic gain control (AGC) target value of 3e6. Up to 15 peptide precursors were isolated (isolation width of 1.7 Th, maximum injection time of 75 ms, AGC value of 1e5), fragmented by HCD using 25 % normalized collision energy (NCE) and analyzed in the Orbitrap at a resolution of 15,000. The dynamic exclusion duration of fragmented precursor ions was set to 30 s.

(Competition) Pulldown assay protein identification and quantification.

Protein identification and quantification was performed using MaxQuant[51] (v 1.6.1.0) by searching the LC-MS/MS data against all canonical protein sequences as annotated in the Swissprot reference database (v03.12.15, 20193 entries, downloaded 22.03.2016) using the embedded search engine Andromeda. Carbamidomethylated cysteine was set as fixed modification and oxidation of methionine and N-terminal protein acetylation as variable modifications. Trypsin/P was specified as the proteolytic enzyme and up to two missed cleavage sites were allowed. Precursor tolerance was set to 10 ppm and fragment ion tolerance to 20 ppm. The minimum length of amino acids was set to seven and all data were adjusted to 1% PSM and 1% protein FDR. Label-free quantification[51] and match between runs was enabled (except for search of experiment corresponding to Fig S1d).

(Competition) Pulldown assay data analysis.

For the competition assays, relative binding was calculated based on the protein intensity ratio to the DMSO control for every single inhibitor concentration. EC_{50} values were derived from a four-parameter log-logistic regression using an internal R script that utilizes the ‘drc’ package in R. The obtained EC_{50} values were multiplied with a protein-dependent correction factor (cf), resulting in the apparent K_d value (K_d^{app}). The correction factor is determined by calculating the ratio of the protein intensity of two consecutive pulldowns of the vehicle control sample[15]. Correction factors were set to the median of correction factors derived from all competition assays (cf^{HDAC1}=0.46, cf^{HDAC2}=0.41, cf^{HDAC3}=0.44, cf^{HDAC8}=0.33, cf^{HDAC6}=0.46,

cf^{HDAC10}=0.42, cf^{HDAC4}=0.54, cf^{HDAC5}=0.36, cf^{HDAC7}=0.60, cf^{ALDH2}=0.38, cf^{ISOC1}=0.39, cf^{ISOC2}=0.32, cf^{GATD3A}=0.46, cf^{MBLAC2}=0.54). Targets of the inhibitors were annotated manually. A protein was considered a target or interactor of a target if the resulting binding curve showed a sigmoidal curve shape with a dose dependent decrease of binding to the beads. Additionally, the number of unique peptides and MSMS counts per condition were taken into account.

Heatmaps were generated using the R package ‘pheatmap’. Initial clustering of drugs for the target landscape was based on the relative affinities using the Euclidian distance measure.

For comparison of the novel affinity matrix iA to control beads and iQ, we used iBAQ intensities (approximation to the absolute amount of proteins) obtained from MaxQuant analysis. We only calculated fold changes for proteins that were detected in all replicates of the iA pulldown. For the iQ and control beads pulldown duplicates with one missing value we imputed the missing value by multiplying the iBAQ intensity of the valid value with the imputation factor of one plus the mean standard deviation over all replicates without missing values (1+mean(SD)), resulting in rather overestimated intensity of the protein in the control sample. To calculate the significance of the fold change, a t-test with Benjamini-Hochberg correction was applied. Proteins that have been identified in every replicate of the iA pulldown but in none of the iQ or control bead pulldown replicates are highly significant enriched targets, but cannot be assigned to actual values. Hence they are listed along an arbitrary high fold change value and set to an arbitrary low p-value for plotting with the other enriched proteins.

For kinetics experiments, we calculated the LFQ-intensity of different drug incubation time points divided by the intensity of the vehicle control PD of the same experiment. This relative binding to the beads was then plotted against the total incubation time (i.e. drug pre-incubation plus pulldown-incubation time) to give the binding kinetics curves.

CATDS score calculation.

The general formula for the calculation of CATDS (Concentration And Target Dependent Selectivity)[20] is:

$$CATDS_{target} = \frac{\sum(target\ engagement)_{targets\ of\ interest}}{\sum(target\ engagement)_{all\ targets}}$$

We use the term target engagement as often done in drug discovery. It refers to the fraction of all protein molecules that are bound by the drug at a particular drug concentration. By that definition, 50% target engagement corresponds to the K_d^{app} of the drug-protein interaction.

In this work, we only ever refer to selectivity at the K_d^{app} of a particular target. This simplifies the calculation as follows

$$CATDS_{target} = \frac{0.5}{\sum(target\ engagement)_{all\ targets}}$$

I our assay, the level of target engagement at any drug concentration of interest can be calculated as “1 – relative residual binding” at that drug concentration. Hence, this is equivalent to:

$$CATDS_{target} = \frac{0.5}{\sum(1 - relative\ residual\ binding)_{all\ targets}}$$

To illustrate this by example, a perfect CATDS score of 1 would mean that the drug only has a single target which is the target of interest. If there are two equipotent targets for a drug, the CATDS score would be reduced to 0.5.

Screen for inhibitor-induced cell morphology.

24 h after seeding SW620 in microtiter-plates at 3×10^3 cells/well, each compound was added in quadruplicates at 1 μM and 0.1 μM concentrations. Morphology of the cells was monitored for 60 h of compound exposure using an automated live cell imaging system (IncuCyte S3, Sartorius, software version v 2009B). The bright light images were processed by ilastik[52], a supervised machine learning image analysis tool kit, in order to assign and quantify different morphotypes. The areas covered by the morphotypes (number of pixels) were used to calculate the fraction of each morphologies in the different wells.

HDAC-Glo assay, HDAC10 TR-FRET assay and BRET assay.

The experiments were performed according to the methods section of R. Steimbach, et al.[53].

Palmitoyl-CoA hydrolysis assay.

MBLAC2 was expressed and purified from insect cells as previously described[14]. Palmitoyl-CoA was purchased from Sigma and stored at a stock concentration of 1 mM in 50 mM MES, pH 7.4 containing 0.05% DDM. [^{3}H]-palmitoyl-CoA was synthesized using [^{3}H-]palmitate (45 Ci/mmol, PerkinElmer Life Sciences), CoA (Sigma), and acyl CoA synthase (Sigma) as described[54].

To screen for MBLAC2 palmitoyl-CoA hydrolase inhibitors, MBLAC2 (30 nM) was incubated with each inhibitor (300 nM) at 30 °C for 10 min. A reaction hot mix (RHM) was prepared by mixing non-radioactive palmitoyl CoA with [^{3}H]-palmitoyl CoA to a final concentration of 6.25 μM (specific activity 4,000 dpm/pmol). The hydrolysis reaction was initiated by adding 200 μL of the RHM to 50 μL of the enzyme:inhibitor solution at 30 °C. The reaction was allowed to proceed for 10 min and then terminated with 0.5 mL of Dole’s reagent (2-propanol:heptane:1 M H_2SO_4, 25:5:1). The [^{3}H]-palmitic acid product was isolated by extraction with 250 μL heptane followed by vigorously shaking for one hour. The organic layer collected was quantified by scintillation spectrometry. To determine the IC_{50} values for selected HDAC inhibitors, various concentrations of each inhibitor (3 μM to 1 pM) were prepared in 50 mM Tris, pH 7.4 prior to incubation with MBLAC2.

Ceramidase Assay.

The ceramidase activity of MBLAC2 was evaluated by monitoring the hydrolysis of a fluorescent ceramide analog, C12-NBD-ceramide (Avanti Polar Lipids) as previously

described[55]. Purified MBLAC2 (1 nM to 1 μM) or native cell lysate was incubated with C12-NBD-ceramide (1 μM) at 37 °C for up to 6 h. The reaction was terminated by boiling followed by solvent evaporation. The lipids were resuspended in 30 μL of chloroform/methanol (2:1, v/v) and applied to a TLC plate, which was developed with chloroform/methanol/25% ammonium hydroxide (90:20:0.5, v/v). Separation of the lipid mixture was visualized with Versadoc Imaging System (Alexa Fluor 488 filter).

Knockdown of MBLAC2 in HEK293 cells.

Transfection was performed using the protocol from siPOOL Biotech (https://www.sitoolsbiotech.com/pdf/siPool%20Transfection%20Protocol.pdf) following the reverse transfection instructions and using a final concentration of 1 nM or 3 nM siRNA-POOL (30 MBLAC2 targeting siRNAs) for knockdown of MBLAC2 or 3 nM control-siRNA (Pool of 30 scrambled siRNAs). Lipofectamine RNAiMAX (Invitrogen, 13778–030) was used as transfection reagent. In brief, siRNAs were pre-diluted in Opti-MEM (Gibco) and combined with a pre-mixed Opti-MEM/RNAiMax dilution, incubated for 5 min at RT and transferred to the bottom of 6-well cell culture plates. Detached HEK293 cells were resuspended in DMEM containing 10% Exosome-depleted FBS (qualified one shot, Gibco, A27208–03) as FBS replacement (to avoid extracellular particle contamination stemming from FBS) and added to the transfection mix in 6-well plates to settle down for 10 min before transfer to the incubator (37 °C, 5% CO_2, cell confluence of 15%). For the knockdown test with western blot readout, cells were incubated for 1,2 and 3 days before lysis. For every treatment duration, cells were transfected with 3 nM control siRNA POOL, 1 or 3 nM MBLAC2 siRNA POOL. For the proteomics and EV-counting experiment (in triplicates), knockdown cells were incubated for 3.5 d after siPOOL transfection, reaching 80% confluency. For lipidomics experiments (in triplicates) transfection and cultivation happened on glass dishes (to avoid plastics-derived contamination during planned lipid-extraction from attached cells).

Treatment of HEK293 for exosome characterization.

HEK293 cells were seeded in 6-well cell culture dishes with a confluence of 15% and cultured in FBS-free DMEM (10% exosome-depleted FBS (Gibco, A27208–03)). After 4h cells were treated with ACY-775 or ACY738 (triplicates, 3 μM final concentration) for 3.5 days.

Extracellular vesicle (EV) sample preparation and EV-counting.

Supernatants of ACY-775, ACY-738 treated and MBLAC2-siPOOL/control siRNA transfected HEK293 cells were collected and stored at −80 °C. Thawed supernatant samples were applied to qEV (35 nm, qEVoriginal, IZON) size exclusion chromatography to collect supernatant samples in the size range of extracellular vesicles. Briefly, the column was first washed and equilibrated with sterile PBS. Then, 1 mL of cell culture supernatant were pipetted onto the column and 0.5 mL fractions were collected in Eppendorf-reaction vessels. The fractions of column flow through (6–8, i.e. 3 – 4.5 mL of flow through after applying sample), that contain most particles in the size range of 30 – 150 nm were were analyzed using a NTA-particle tracker. Measurement of particle number and size distribution of EVs was performed using the scatter mode of a PMX110-Z ZetaView Nanoparticle Tracking Analyzer by Particle Metrix, equipped with a 520 nm laser. Two video cycles were recorded

over all 11 positions in the measurement cell while the temperature was held constant at 24 °C. The following recommended parameters were used for the measurement: Sensitivity (80), Shutter (70), Frame rate (30), Min. Brightness (20), Max. Brightness (255), Min. Area (5), Max. Area (1000), Tracking radius (100), Min. Tracelength (15), nm/class (5) and classes/decade (64). Results were analyzed using the ZetaView Software Version 8.05.12 SP1 by Particle Metrix.

Extracellular vesicle count data analysis.

The particle count data from NTA (binned in 5 nm diameter) for each fraction (6/7/8, fraction 7 containing most particles) of a replicate were summed up and normalized to the protein concentration of the corresponding replicate (as approximation for the cell volume; concentration determination by BCA assay, see below). The normalized particle size distributions of the replicates were plotted using GraphPad PRISM (v5.01).

Western blot.

Protein lysates were generated by harvesting cells in lysis buffer (0.8% NP40, 50 mM Tris-HCl pH 7.5, 5% glycerol, 1.5 mM $MgCl_2$, 150 mM NaCl, 1 mM Na_3VO_4, 25 mM NaF, 1 mM DTT and supplemented with protease inhibitors (SigmaFast, Sigma) and phosphatase inhibitors (prepared in-house according to Phosphatase inhibitor cocktail 1, 2 and 3 from Sigma-Aldrich)). The protein amount of cell lysates was determined by Bradford assay. Proteins were separated by SDS-PAGE and electro-transferred onto PVDF membranes. Blots were stored in Tris-buffered saline, supplemented with 0.05 % Tween (TBS-T) and 4 % BSA for 1 h at room temperature and then incubated with primary antibody diluted in 1xTBS,0.05 % Tween and 4% BSA overnight at 4 °C. Following antibodies were used for MBLAC2 probing: MBLAC2 (Abcam #ab122411, 0.2 mg/mL, rabbit polyclonal IgG; diluted 1:250) and beta-Actin (Santa Cruz Biotechnology #sc-47778, 0.2 mg/mL, monoclonal mouse IgG, diluted 1:500). For Acetyl-Tubulin probing, following antibodies were used: Acetyl-alpha-Tubulin (Lys40) (Cell Signaling Technology, #12152S, monoclonal mouse IgG, diluted 1:750), and beta-Actin (Cell Signaling Technology, #8457S, monoclonal rabbit IgG, diluted 1:750). After antibody incubation, blots were washed in TBS-T and probed with the corresponding fluorophore-conjugated secondary antibody (ODYSSEY donkey-anti-rabbit (#926–68023), goat-anti-mouse (#926–32210)) for 3 h at room temperature. The immuno-reactive signals were detected by excitation of the respective fluorophore. Acquisition and quantification of the band intensities was carried out with the Odyssey (Licor) imaging system and corresponding software (v 3.0.29). Intensities of proteins were normalized to input beta-Actin. For the MBLAC2 western blot, intensities were further normalized to the control siRNA POOL transfected samples of each treatment duration to calculate the relative MBLAC2 knockdown after 1,2 and 3 days of transfection.

Deep proteome sample preparation

Protein Digestion.

After 3.5 days of transfection or drug treatment, HEK293 cells were washed with PBS and lysed by adding 100 µL lysis buffer (4% SDS in ddH_2O) before scraping cells off the surface. Lysates were transferred to 2 mL eppendorf reaction vessels. To hydrolyse

DNA and reduce viscosity, lysates were first diluted with 500 µL lysis buffer, heated at 95 °C for 10 min and then mixed with trifluoroacetic acid (TFA) to a final concentration of 2%. Next, N-methylmorpholine (Sigma) was added to 4% (v/v) final concentration for neutralization. Protein concentration of lysates was determined using a standard BCA-assay protocol (Pierce™ BCA Protein Assay kit, #23225).

Protein cleanup and digestion was performed according to an adapted SP3 protocol. In brief, lysate volumes corresponding to 42 µg of protein were added to 5 µL Sera-Mag beads 1:1 mix (cat# GE45152105050250 and GE65152105050250, GE Healthcare) before adding ethanol to a final concentration of 80% (v/v) and incubating at RT for 15 min under constant shaking (800 rpm). Beads were then immobilized to reaction vessel wall by magnets and washed twice with 1 mL of 80% ethanol and once with 80% acetonitrile. Beads were resuspended in 70 µL of 50 mM HEPES buffer (pH = 8.5) and incubated with Dithiothreitol (DTT) (10 mM final concentration, 45 min at 37 °C, 600 rpm shaking) for reduction. Proteins were alkylated by adding chloroacetamide to a final concentration of 55 mM (30 min at RT, 600 rpm shaking in the dark). To digest the proteins, trypsin was added (trypsin:protein = 1:50) and incubated with beads at 37 °C and 800 rpm shaking for 16 h. Digested protein peptides were collected by immobilizing beads on vessel walls using magnets and transferring the peptide solution to eppendorf reaction vessels.

StageTip Desalting.

To construct a StageTip, six C18 disks were packed into a 200 µL pipette tip. The StageTips were activated with 200 µL acetonitrile (centrifugation at 1000 g), followed by washing with 200 µL Buffer B (0.1 % formic acid in 50 % acetonitirile) at 1000 g and equilibration by washing with 200 µL Buffer A (0.1% formic acid in ddH_2O) at 1000 g. Peptide samples were acidified to a final concentration of ca. 1% formic acid (pH > 2) and loaded on StageTips with 500 g centrifugation. The loading step was repeated with the flow through. Peptides attached to the C18 material were washed twice with 200 µL buffer A and eluted by adding twice 40 µL of buffer B and collecting the flow through. The eluent was frozen at −80 °C and vacuum dried before further processing.

TMT labelling.

Samples were reconstituted in 20 µL of 50 mM HEPES (pH = 8.5) and labelled with 100 µg (5 µL of 20 µg/µL) TMT10plex (Thermo Scientific, channel 126 was used for MBLAC2-KD and 127N was used for control replicates) for 1 h at 25 °C under 500 rpm constant shaking. The labelling reaction was stopped by adding 3 µL 5% Hydroxylamine in ddH_2O. After combining TMT labelled samples in reaction vessel they were acidified with 20 µL of 10 % formic acid in ddH_2O. Samples were frozen at −80 °C and vacuum dried before further processing.

High-pH RP-HPLC fractionation.

In brief, the pooled TMT-labelled peptides were reconstituted in 50 µL Buffer A (25 mM ammonium bicarbonate, pH = 8) and separated using a Dionex Ultra 3000 HPLC system (Dionex Chromeleon (v.6.80) software) equipped with an Waters XBridge BEH130 C18 3.5 µm column (2.1 × 150 mm) operated at a flow rate of 200 µl/min with a constant 10%

of 25 mm ammonium bicarbonate (pH = 8.0) in the running solvents. A 57 min linear gradient from 7 to 45% ACN in ddH2O followed by a 6 min linear gradient up to 80% ACN was employed. Ninety-six Fractions were collected and subsequently pooled to 48 fractions (fraction 1 + 49, fraction 2 + 50, and so on). Peptide fractions were frozen at −80 °C and dried by vacuum centrifugation.

Full proteome LC-MSMS.

Peptides were analyzed via LC-MS/MS on a Dionex Ultimate3000 RSLCnano System equipped with a Vanquish pump module coupled to an Orbitrap Fusion Lumos (Thermo Fisher Scientific) mass spectrometer. Peptide fractions were dissolved in 1% FA and injected directly onto a commercially available Acclaim PepMap 100 C18 LC column (2 μm particle size, 1 mm ID × 150 mm; Thermo Fisher Scientific). Peptides were separated using a 25 min linear gradient ranging from 4–32 % solvent B (0.1 % formic acid, 3% DMSO in acetonitrile) in solvent A (0.1 % formic acid, 3% DMSO in HPLC grade water) at a flow rate of 50 μL/min.

The mass spectrometer was operated in data dependent mode, automatically switching between MS1, MS2 and MS3 spectra, with cycle time set to 1.2 s. MS1 spectra were acquired over a mass-to-charge (m/z) range of 360–1560 m/z at a resolution of 60,000 in the Orbitrap (OT) using a maximum injection time of 50 ms, an automatic gain control (AGC) target value of 4e5 and dynamic exclusion set to 50 s.

For MS2 spectra, the intensity threshold was set to 1E4, default charges were set to state 2–6. The isolation width was set to 0.6 m/z and HCD collision energy [%] was set to 32. The AGC target value was 1.2E4, and the first mass was fixed at 100 m/z. The Iontrap was used to detect the MS2 spectra with the rapid scan function. The maximum injection time was 40 ms. Regarding MS3-Filter, precursor selection range was set to 400–2000 and exclusion mass widths were set to 20 m/z for low and 5 m/z for high. For MS3 scans, Synchronous precursor selection was enabled, the number of SPS precursors was set to 8, the MS isolation window was 1.2 m/z, and HCD collision energy was 55%. The Orbitrap was used to detect the MS3 spectra at 50,000 resolution and over a scan range of 100–1000. The AGC target was 1E5 with a maximum IT of 86 ms.

The raw data was analyzed using MaxQuant (version 1.6.10.2) and default settings, except for minor changes: Isotope impurities of the TMT lot (#TE268169) were specified to allow MaxQuant the automated correction of TMT intensities. TMT-labelling modification was set for Lysine and N-terminal aminogroups and ITMS was set to a match tolerance of 0.4. For all searches, carbamidomethylated cysteine was set as fixed modification and oxidation of methionine and N-terminal protein acetylation as variable modifications. Trypsin/P was specified as the proteolytic enzyme with up to two missed cleavage sites allowed. Searches were based on canonical Swissprot reference database (v03.12.15, 20193 entries, downloaded 22.03.2016, annotated in-house with PFAM domains).

Full proteome data analysis.

For data analysis and visualization, mostly Microsoft Excel, GraphPad Prism (v5.01), RStudio (version [4.0.2]), and the Perseus software (v. 1.6.2.3) were used[56]. Firstly, all

reversed hits and “only identified by site” protein entries were removed from the MaxQuant output. Then, the reporter intensities of channels 1,2 and 5 (i.e. TMT126, TMT127N, and TMT128C; corresponding to MBLAC2 knockdown, control siPOOL transfection and DMSO control) were log2 transformed and median-centered to the overall median of the respective dataset. Further, samples were adjusted with ComBat[57] from the śvá package (version [3.30.1]) to remove batch effects between replicates. Protein groups without missing values were analyzed in Perseus[56] (v1.6.2.2) by using the built-in two-sample t-test function and Benjamini-Hochberg multiple-testing correction (MBLAC2/control, S0 = 0.107, FDR = 1%). Resulting table containing fold changes, p and q values was exported and used to plot volcano plots in GraphPad PRISM (v5.01).

Lipidomics sample preparation.

HEK293 were cultured on glass dishes for 45 h after transfection in DMEM (containing 10% exosome depleted FBS, Gibco, A27208–03) until they reached a confluency of 80%. The supernatant was discarded and cells were gently washed with PBS. For Lipid extraction, 500 μL of 2:1 (v:v) Methanol:Chloroform was pipetted twice onto cells in the glass dish and broken up cell fragments were collected in glass vials and sonicated for 10 min. After centrifugation to remove cell debris, extracted lipids were stored in extraction buffer at −80 °C until injection to LC-MSMS.

Lipidomics LC-MSMS measurement.

The lipid analysis was performed using a Nexera UHPLC system (Shimadzu) coupled to a Q-TOF mass spectrometer (TripleTOF 6600, AB Sciex) according to a published analytical method[58]: Separation of the lipid extract was performed using a UPLC BEH C18 2.1×100, 1.7 μm analytical column (Waters Corp.) with 300 μL/min flow rate. The mobile phase was water/acetonitirile (40:60, v:v) with 10 mM ammonium formate and 0.1% formic acid (eluent A) and isopropanol/acetonitirile (90:10, v:v) with 10 mM ammonium formate and 0.1% formic acid (eluent B). The gradient profile was 32% B from 0 to 1.5 min raising to 97% B at 21 min, which was held for 4 min. Afterwards, the column was equilibrated at starting conditions. A volume of 5 μL per sample was injected. The autosampler was cooled to 10 °C and the column oven heated to 40 °C. The samples have been measured in the Information Dependent Acquisition (IDA) mode. MS settings in the positive mode were as follows: Gas 1 55, Gas 2 65, Curtain gas 35, Temperature 500 °C, Ion Spray Voltage 5500, declustering potential 80. The mass range of the TOF MS and MS/MS scans were 100 – 2000 m/z and the collision energy was set to 35 V with a 15 V spread. MS settings in the negative mode were as follows: Gas 1 55, Gas 2 65, Cur 35, Temperature 500 °C, Ion Spray Voltage −4500, declustering potential −80. The mass range of the TOF MS and MS/MS scans were 100 – 2000 m/z and the collision energy was set to −35 V with a 15 V spread.

Lipidomics Data analysis.

Data was analyzed using MS-DIAL4[59] software (ver. 4.38). Raw files from positive and negative ion mode were analyzed separately and loaded as lipidomics profile data type. Changes or specifications regarding the default parameter settings were: Defining solvent type as $HCOONH_4$, allowing all adduct types for all lipid classes for identification, and selecting adduct types for positive mode ($[M+H]^+$, $[M+NH4]^+$, $[M+Na]^+$) or negative mode

($[M-H]^-$, $[M-H2O-H]^-$, $[M+FA-H]^-$). Data from knockdown and control were aligned as class and normalized using the mTIC normalization function of MS-DIAL4. The raw MS-DIAL4 outputs for negative and positive mode were processed separately. Lipids that were present in less than half the samples or which showed a retention time of less than one minute were discarded. Additionally, only the lipids that were identified based on their MS2 spectrum were included in the further analysis. Quotient normalization[60] as well as log2 transformation was applied to the data. For the volcano plots the log2 fold change between control and knockdown was calculated and a t-test was performed. The resulting p-values were adjusted for multiple testing using the Benjamini-Hochberg procedure supplied by the statsmodels package. For visualization, t-test results of positive and negative mode data were combined and presented in a volcano plot generated in GraphPad Prism. Since some detected fragment ions were very low abundant in positive ion mode, we decided to remove acyl chain information and only use the sum species annotation for lipids identified in positive mode (Fig. 5c, Supplementary Data 4).

Data Availability.

Chemoproteomics data are freely accessible on ProteomicsDB.org. The mass spectrometry proteomics data including the used Swissprot reference database have been deposited to the ProteomeXchange Consortium via the PRIDE partner repository with the dataset identifier PXD026657. The untargeted metabolomics data for lipidomics are made available on MetaboLights repository with the identifier MTBLS3557 and can further be accessed on Zenodo (https://zenodo.org/record/5914128#.Yfe59_jTVhE).

Extended Data

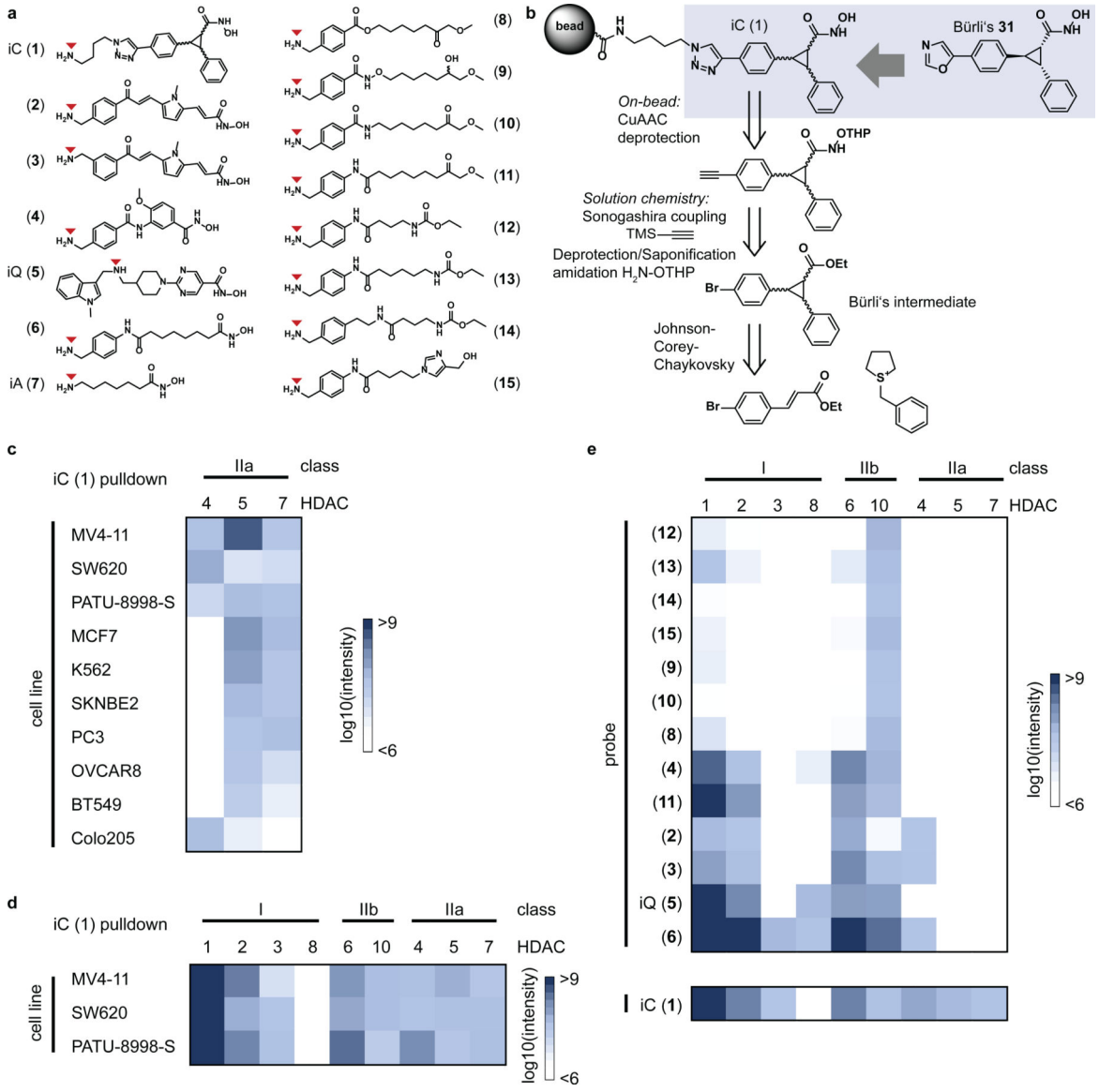

Extended Data Fig. 1. Evaluation of affinity probes for capturing HDACs in cancer cell lysates.

a, Structures of synthesized HDAC affinity probes 1–15. Positions for on-bead immobilisation are marked with red triangles. Probes **2** and **3** are respectively *para* and *meta* linkable analogues of reported class IIa inhibitor MC1568[1]. Probe **4** is an analogue of a HDAC8 inhibitor[2, 3]. Probe **6** is a linkable analogue of Vorinostat[4]**. 8-15** feature alternative chelating groups to hydroxamate, grafted on hybrid structures of Vorinostat, Santacruzamate and LMK235: methoxymethyl ketone (8, 10, 11) found in a bicyclic tetrapeptide[5], ethyl carbamate (12, 13, 14) found in Santacruzamate[6] and 4-hydroxymethylimidazole (15) computationally suggested as superior to hydroxamic acid[7]. **b**, Strategy and retro-synthesis scheme for the design and preparation of class IIa affinity probe iC (**1**). The analogation of lead oxazole **31**[8] to a triazole allows for immobilisation on Sepharose beads. The matrix is conveniently obtained by on-bead Copper-catalysed Azide-Alkyne Cycloaddition

(CuAAC) of a hydroxamate-protected alkyne precursor with azide-functionalised beads, followed by deprotection. The alkyne precursor was prepared by converting Bürli's bromo ester intermediate in 3 steps: Sonogashira coupling with TMS-acetylene, simultaneous deprotection/saponification and conversion to protected hydroxamic acid. An almost equimolar mixture of 3 enantiomer pairs (only all-*cis* isomers are not obtained during the Johnson-Corey-Chaykovsky synthetic step) constitute iC. (See Supporting Note) **c**, Screening cancer cell lines for class IIa HDAC expression using iC affinity probe. The heatmap depicts the average protein intensity of class IIa HDACs pulled down by iC (MS raw intensity). **d**, Intensities of HDACs pulled down by iC from three most promising cell lines from a different lysis batch. **e**, Evaluating HDAC affinity matrices for HDAC pulldown capabilities. The heatmap shows protein intensities of pulled down HDACs by 14 distinct affinity probes using cell lysate mixes of MV4–11 and SW620. For probes 2–15 a 1:1 mix of SW620 and MV4–11 cell lysate was used, while the heatmap for probe 1 represents an average of detected protein intensities from 2 single pulldowns in SW620 and MV4–11 cell lysate. All pulldowns were performed in three technical replicates.

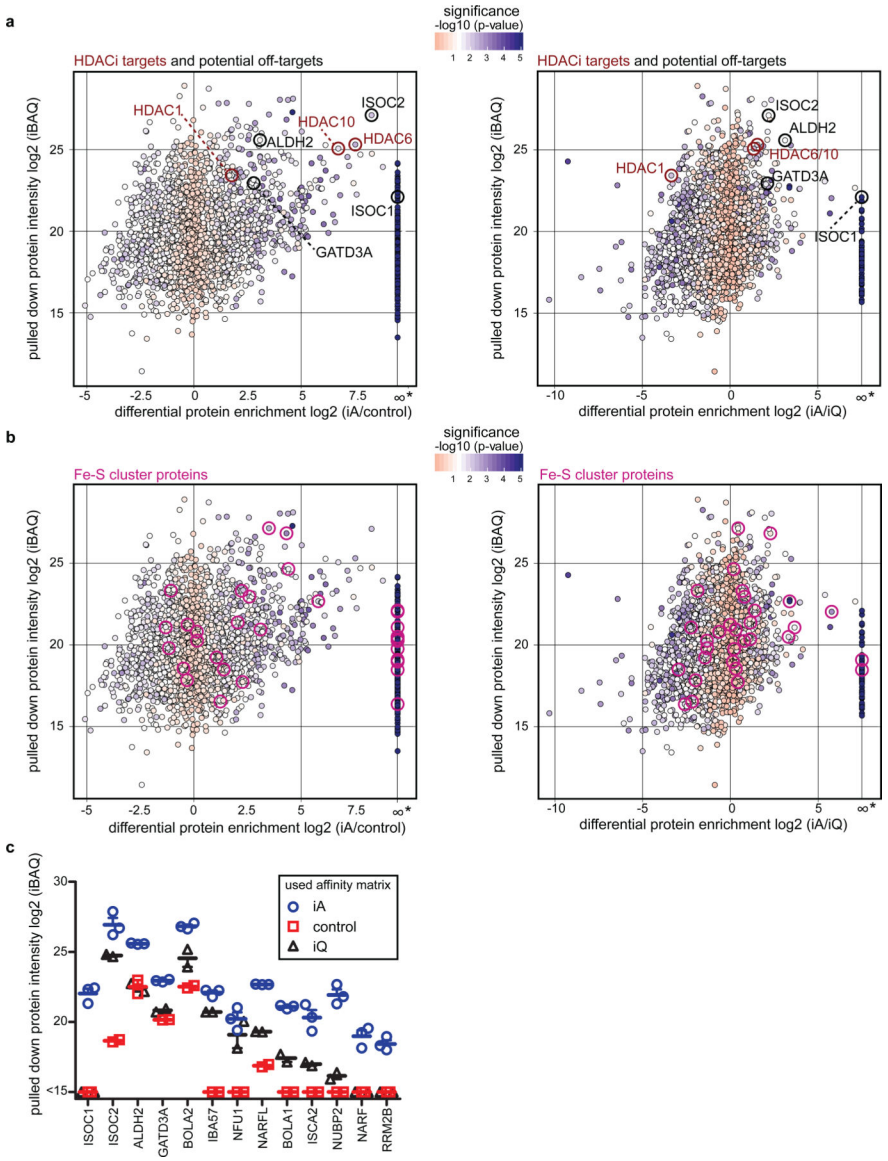

Extended Data Fig. 2. Evaluation of metalloprotein affinity matrix iA for pulling down metalloproteins.

a and **b,** enrichment of proteins from PATU-8998-S lysate by iA relative to control beads or iQ is plotted against the intensity of the corresponding proteins in iA pulldown. iBAQ intensity values were employed as proxy for the protein amount. Asterisks on the x-axis mark proteins that have been identified in each replicate of the iA pulldown but in none of control or iQ replicates and thus represent highly significantly enriched proteins. **a**, enriched HDACs and proposed off-targets are highlighted (two sided t-test, p value without multiple testing correction). **b**, differential chemoproteomic enrichment of FeS-cluster proteins (pink circles) as an example for iA-enriched metalloprotein classes compared to control beads and iQ (two sided t-test, p-value without multiple testing correction). **c**, iBAQ intensities of selected significantly enriched proteins from the single pulldown experiments. All pulldowns were performed in technical replicates (duplicates for control and iQ, triplicates for iA) and data are shown as mean +/− SEM. As control beads we used the same

sepharose beads for affinity matrix generation, but, instead of affinity probes, we coupled 2-aminoethanol to the NHS-activated Sepharose.

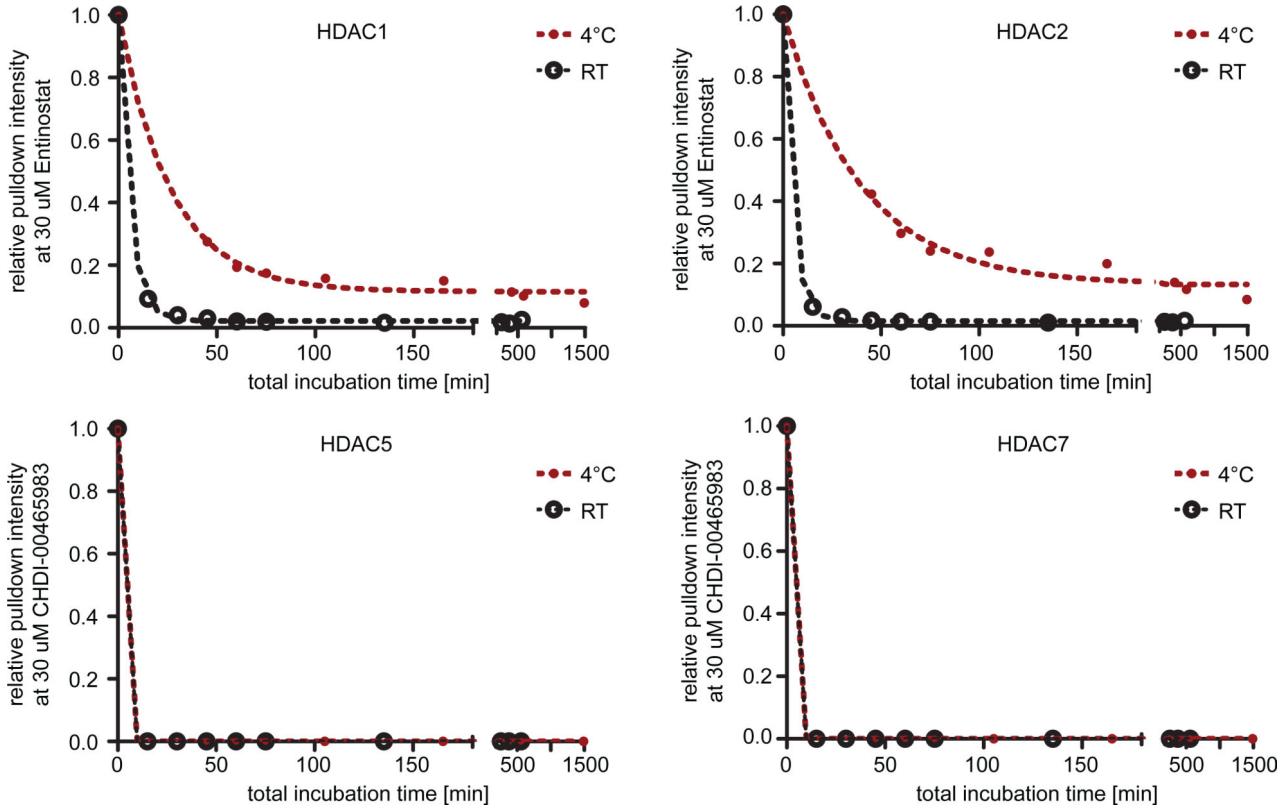

Extended Data Fig. 3. Evaluation of binding kinetics at different incubation temperatures for Entinostat and CHDI00465983.

A 1:1 mix of SW620 and MV4–11 cell lysate was incubated with excess drug (30 μM) for different periods of time at either room temperature (22 °C) or 4 °C before pulling down HDACs with iQ (for Entinostat) or iC (for CHDI00465983). HDAC1 and HDAC2 competition depends on the incubation temperature and Entinostat shows relatively slow binding kinetics compared to CHDI00465983.

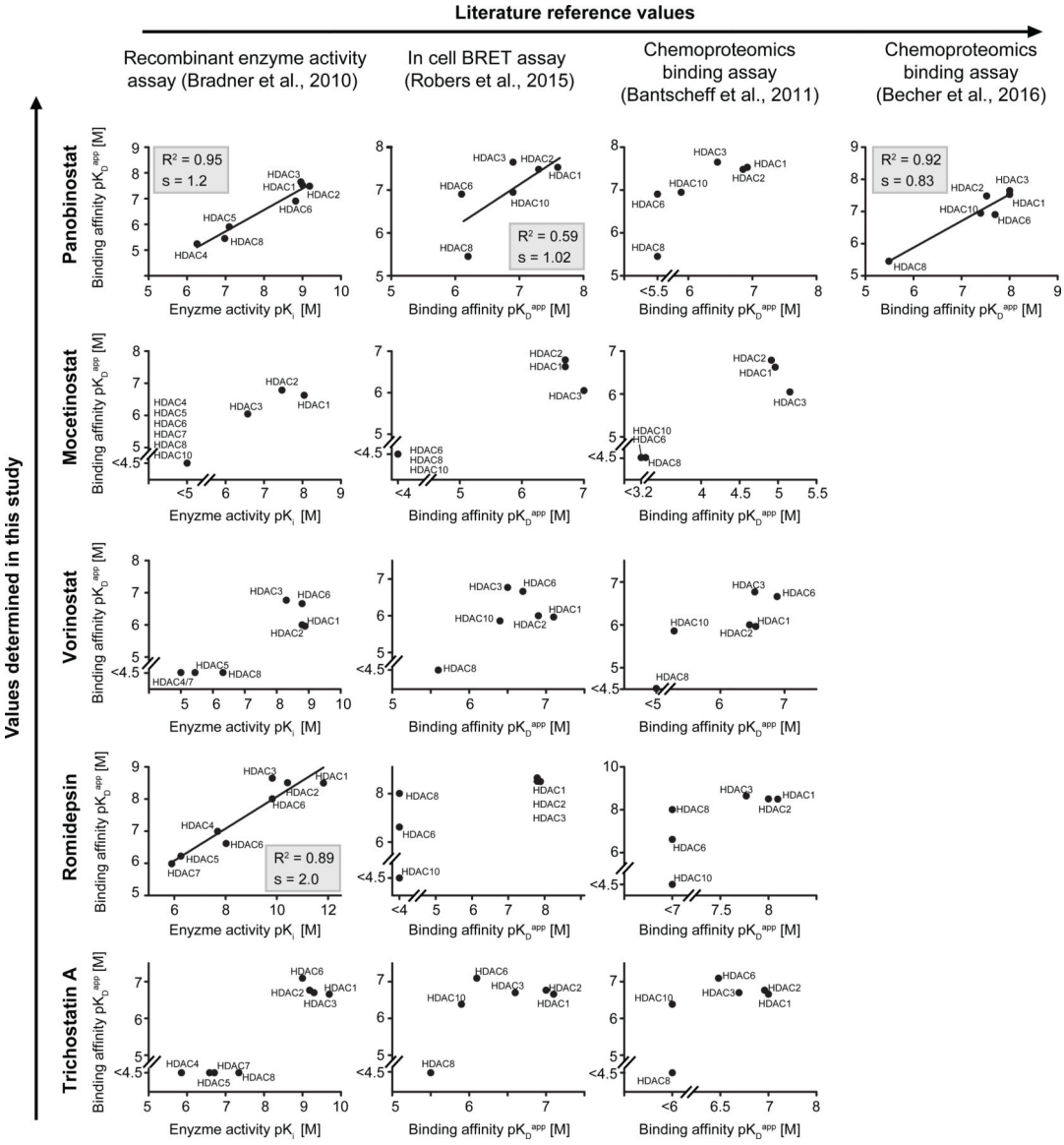

Extended Data Fig. 4. Comparison of acquired affinity data to literature data.

pK_d^{app} values determined in this study were plotted against pK_d values from three former HDACi profiling studies[4, 9, 10] and in case of Panobinostat to another optimized chemoproteomics study using immobilized Panobinostat as probe[9]. For data sets without missing values, regression lines were plotted (s = slope of regression line). In general good correlation is observable between recombinant enzyme activity assay data (Bradner et al.)[10] and our study as well as for the comparison to the optimized chemoproteomics assay using immobilized Panobinostat as affinity matrix (Becher et al.)[9].

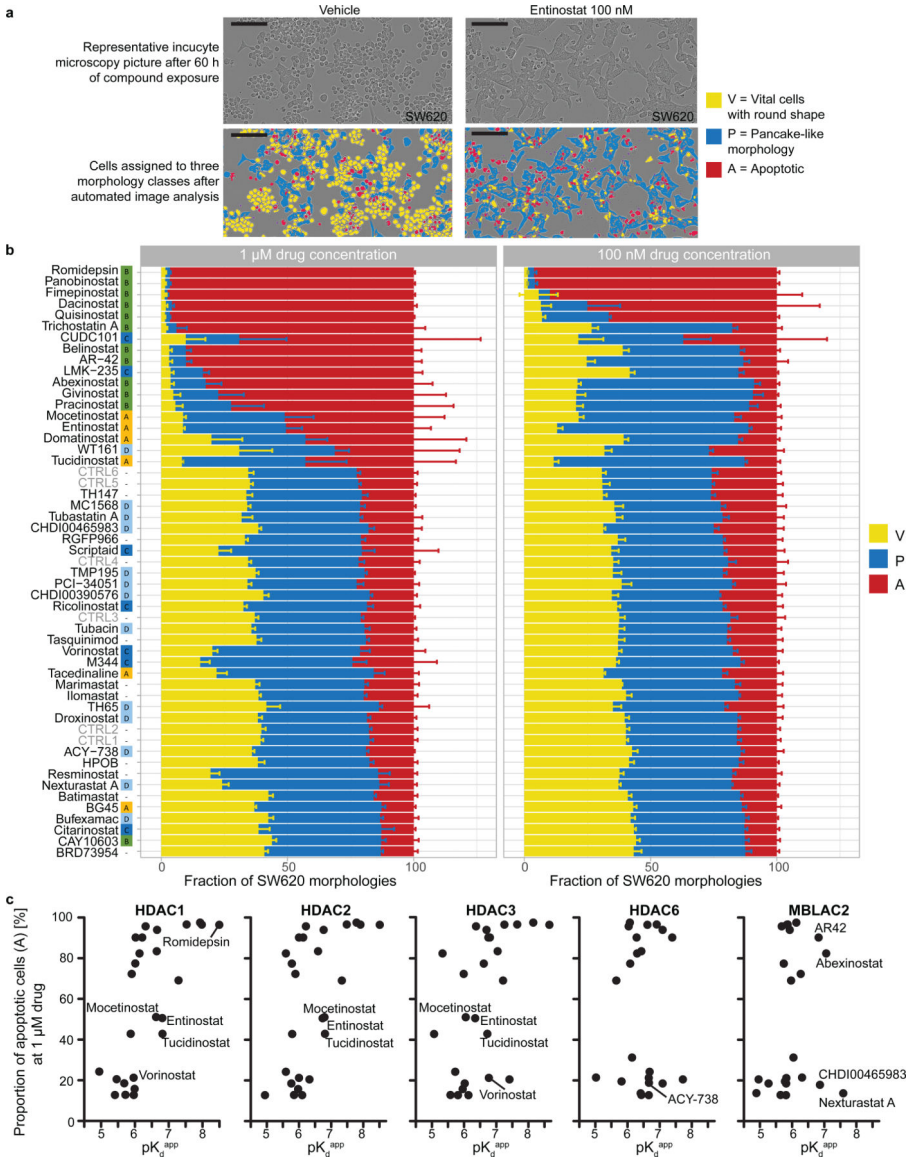

Extended Data Fig. 5. 2-Dose cell viability and morphology screen with HDACi library on SW620 cells

a, Representative images of vehicle (DMSO) and drug treated cells (100 nM Entinostat) after 60 h of incubation. Bright light images (upper panel) were recorded using an Incucyte S3 and processed by ilastik[11], a supervised machine learning toolkit for automated image analysis. Vital round shaped (V), flattened/pancake-like shaped (P) and apoptotic cell morphologies (A) were identified and labelled accordingly (lower panel). Scale bar corresponds to 100 µm length. **b**, Relative areas covered by the the three cell morphologies after drug treatment, performed in quadruplicates. Pixels of the ilastic software output classification were counted and divided by the sum of all cells pixels: bar chart displays the means and standard deviations of quadruplicate experiments in 96-well plates. Treatments were ranked from highest to lowest cytotoxicity (i.e. high proportion of apoptotic cells (A) for the 100 nM and 1 µM treatment). Control DMSO treatments are listed as CTRL1–6. Drugs are assigned to groups according to their target spectrum (see Fig.

2c). **c**, Correlation between drug affinities (pK_d^{app} of HDAC1,2,3,6 and MBLAC2) and proportion of apoptotic cells after 1 μM drug treatment. Representative clinical drugs Romidepsin (depsipeptide), aminoanilides (Mocetinostat, Entinostat, Tucidinostat) and hydroxamates (Vorinostat, AR-42, Abexinostat) as well as some particularly interesting tool compounds (ACY-738, Nexturastat A, CHDI00465983) are highlighted in the plots for orientation. In accordance to literature, class I inhibition correlated with cytotoxicity, while HDAC6 and MBLAC2 inhibition does not correlate with cytotoxicity but clusters into two clouds, defined by the drugs additional class I target affinity (cytotoxicity mainly mediated by class I inhibition). As expected, drugs of similar class I target affinity show distinct cytotoxicity, most probably reflecting distinct intracellular drug concentrations (e.g. via cellular uptake, metabolism, active export). Chemically similar drugs (Mocetinostat, Entinostat, and Tucidinostat) that share the same target space and most probably similar intracellular distributions according to their similar physicochemical properties cluster together.

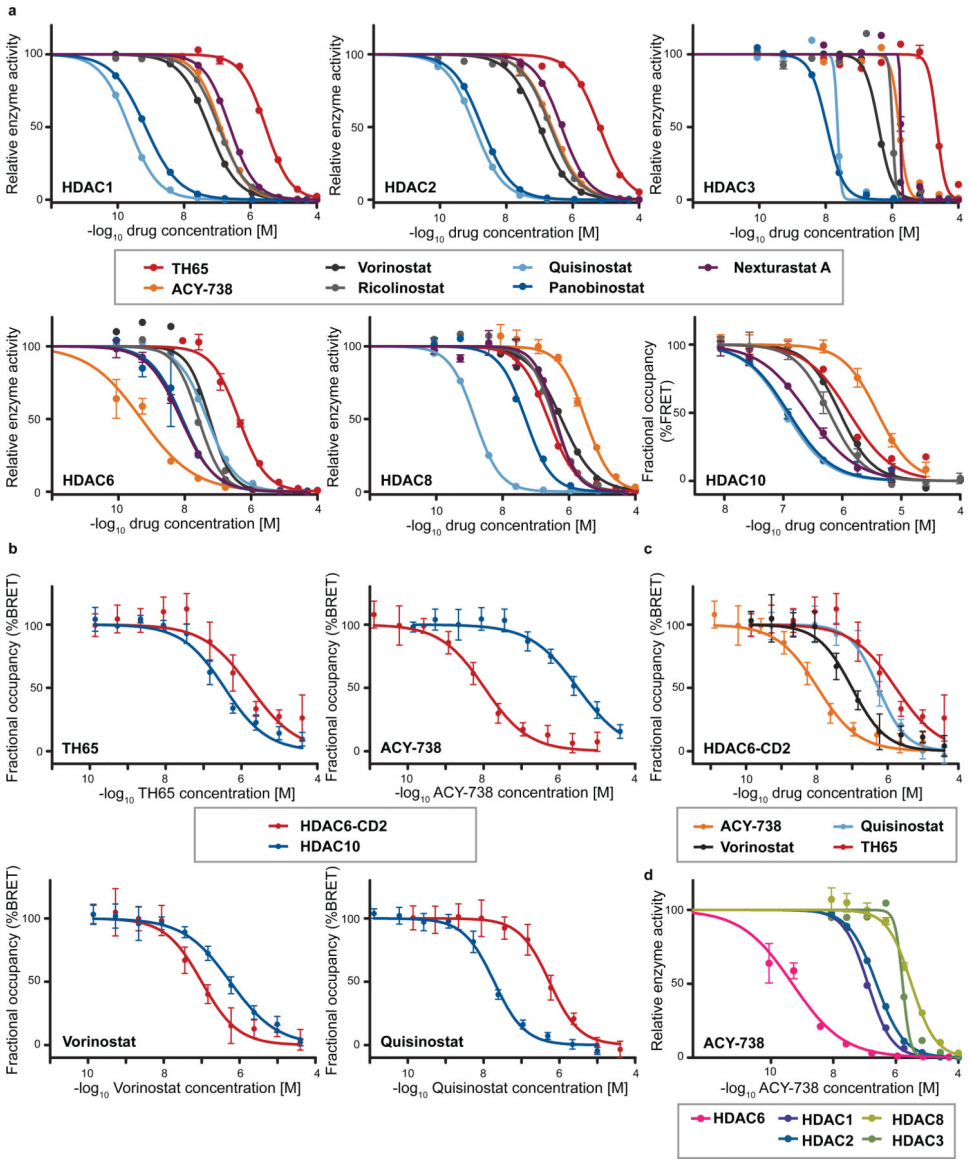

Extended Data Fig. 6. Confirming selectivity of ACY-738 (HDAC6i) and TH65 (HDAC10i) with orthogonal biochemical assays.

a, Dose-dependent in vitro HDAC activity assays were performed using the HDAC-Glo assay for HDAC1/2/3/6/8. In vitro HDAC10 target engagement was determined by the TR-FRET assay (mean of triplicates with SD). **b** and **c**, HDAC6 and HDAC10 nano-BRET assays for in-cellulo target engagement measurement were performed with the selective compounds TH65 and ACY738 as well as with Vorinostat and Quisinostat for comparison. Of note, the HDAC6 nano-BRET only determines in-cell binding affinity to HDAC6 catalytic domain 2 (CD2) and not to CD1. **d**, Dose-dependent in vitro activity assay data for ACY-738 as determined by the HDAC-Glo assay shows the selectivity of ACY-738 over class I HDACs 1/2/3/8. a, d: HDAC-Glo assay was performed in three replicates; b, c: TR-FRET assay was performed in six replicates. Data are presented as mean values +/− SD.

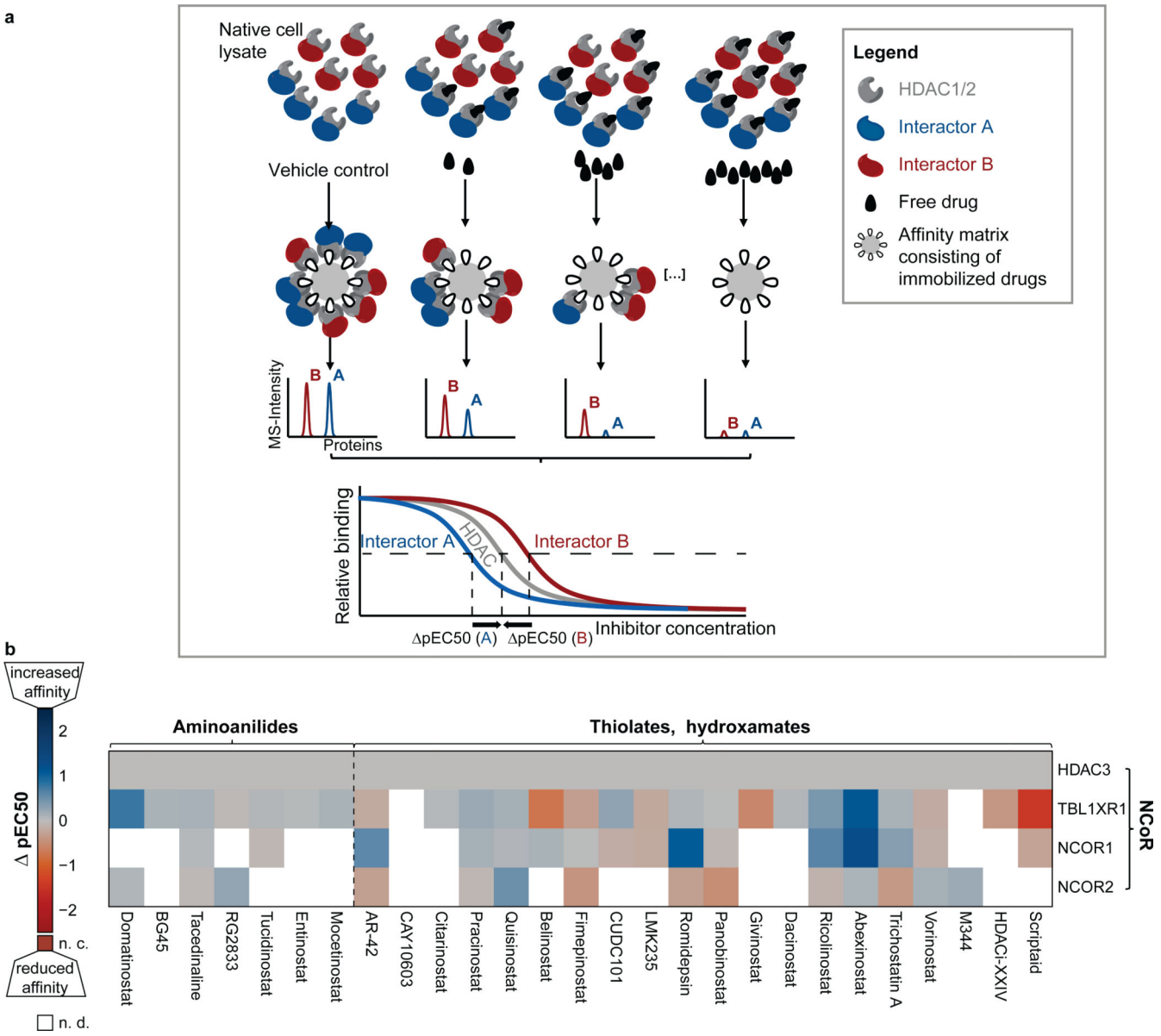

Extended Data Fig. 7. Complex selectivity of class I HDACis.

Schematic representation of acquiring HDAC complex selectivity data. Different interaction partners of the same HDAC (Interactor A and B) can impact the binding affinity of drugs to the HDAC target enzyme, for instance by inducing conformational changes. Since HDACs are bound by competing drugs or affinity probes when in complex with their interactors, all the complex partners show dose-response curves. These curves allow to infer the affinity of drugs to HDACs in complex with the respective interactor (A/B). As a result, the observed curve for the corresponding HDAC is an aggregation of all the potential complex variants and single HDACs, which are not part of complexes. **b,** Complex selectivity map for class I HDACis. The colours of the heatmap indicate differences in affinity to HDAC3 (ΔpEC_{50}) depending on its interaction partners of the NCoR complex. Colour shades of blue show that HDACi affinity is increased upon interaction between HDAC3 and the

corresponding interaction partner, red shades indicate that HDACi loses binding affinity to HDACs interacting with the corresponding interaction partner (Blank space: lack of robust protein quantification prevents precise EC_{50} value determination).

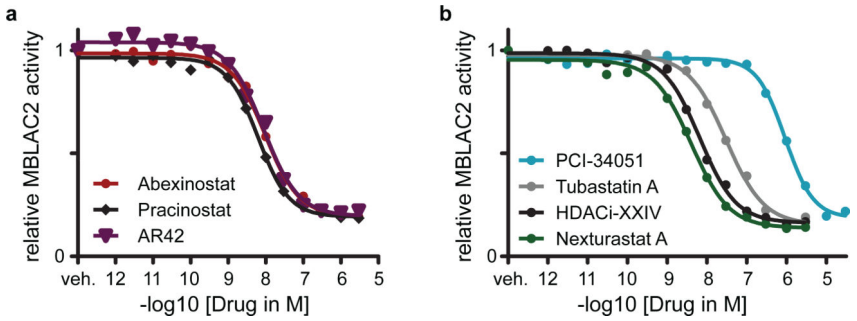

Extended Data Fig. 8. Dose dependent inhibition of MBLAC2 hydrolase activity by HDAC inhibitors.

a, Clinical drugs Abexinostat, Pracinostat and AR-42 all show EC_{50} inhibition values below 10 nM (assay threshold). **b**, Tool compounds and pre-clinical drugs also engage with MBLAC2. While potent MBLAC2 binders from the chemoproteomic profiling show inhibition with nanomolar affinities, PCI-34051 (non-binder chemoproteomic assay) shows over 100-fold lower activity against MBLAC2 (pEC_{50} = 6.0).

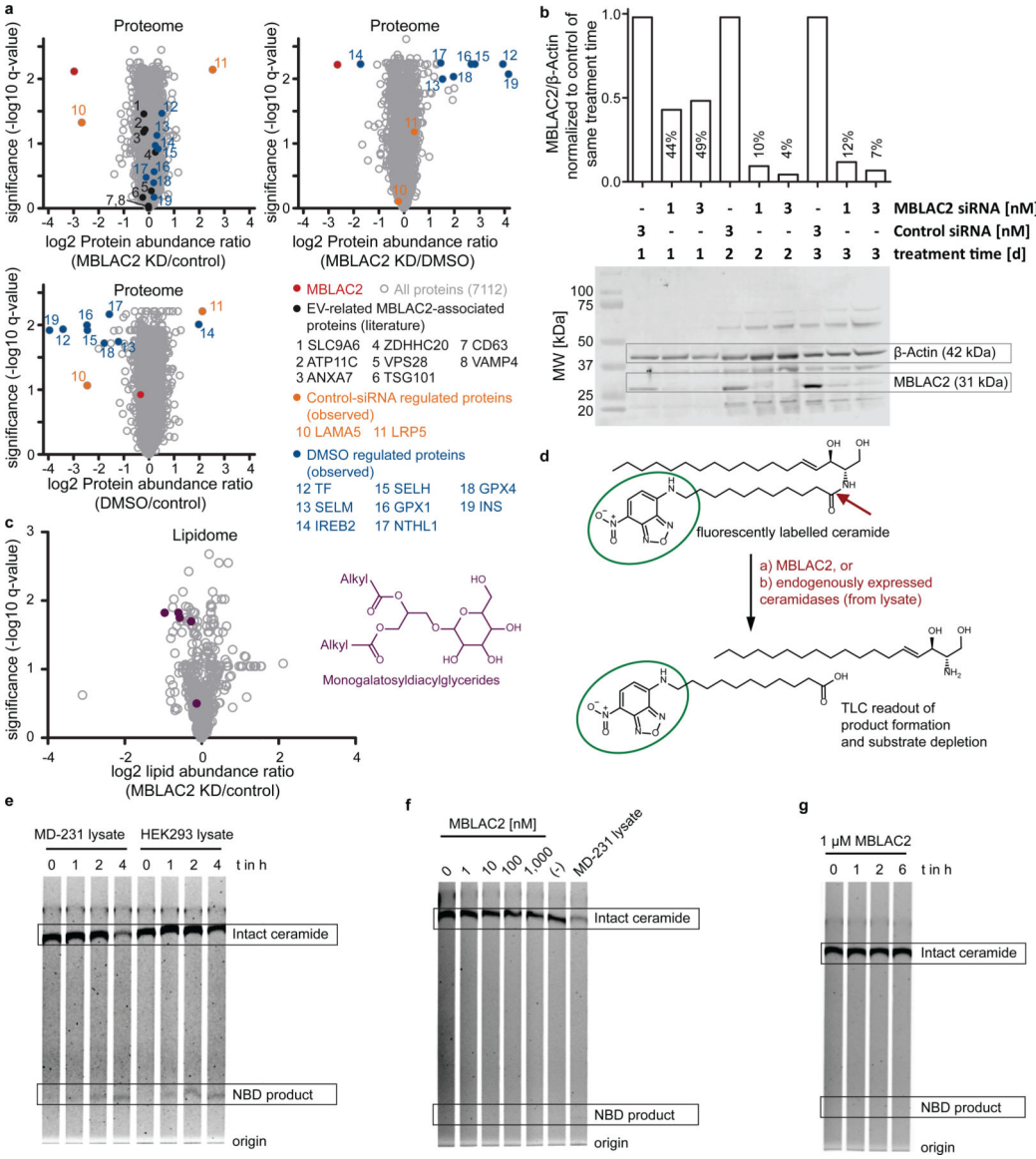

Extended Data Fig. 9. MBLAC2 inhibition and knockdown effects on proteome and lipidome.

siRNA-mediated MBLAC2 knockdown does not lead to major changes of intracellular protein levels. Volcano plots display the difference in protein abundances of HEK293 cells after DMSO treatment of transfection with MBLAC2-directed siPOOL or control siPOOL (biological triplicates). HEK293 were lysed and submitted to a deep bottom-up proteomics workflow, including SP3-bead protein digestion protocol and TMT-labelling for robust quantification. While MBLAC2 knockdown is still efficient 3.5 d after transfection with siRNA POOL (13% compared to control siRNA), the whole proteome is generally unaffected. Intracellular levels of proteins involved in extracellular vesicle biogenesis and associated to MBLAC2 do not change significantly (labelled in grey are potential interaction partners or co-regulated proteins TSG101, ATP11C, SLC9A6, VAMP4, ZHHDC20, CD63, ANXA7, VPS28). We attribute the apparent LRP5 upregulation and LAMA5 downregulation (orange) to effects caused by transfection with control siRNA,

since they are only affected in control siRNA pool treated cells. In analogy, proteins marked in blue are only regulated in DMSO treated cells and therefor attributed to DMSO-related effects (e.g. oxidative mechanisms). **b**, Western blot against human MBLAC2 (and beta-Actin as loading control), showing knockdown efficiencies in dependence of transfection amount and duration. Bands were quantified with the Licor software (see methods) and normalized to the loading control. This normalized MBLAC2 expression was then again normalized to control siRNA treated cells of corresponding knockdown duration to give a relative and time-dependent knockdown efficiency of MBLAC2. In concordance with the full proteome data, knockdown is still sufficient three days after transfection. **c**, MBLAC2 knockdown leads to abundance changes of intracellular lipid families. MBLAC2 knockdown leads to global intracellular downregulation of monogalactosylceramides (general structure scaffold indicated) in HEK293 cells. Volcano plot shows the ratio and statistical significance (q-value) of lipid quantities between MBLAC2 knockdown (MBLAC2-KD - siRNA POOL in triplicate) and control (control siRNA in triplicate), as measured by mass-spectrometry based lipidomics, after MeOH/CHCl3 lipid extraction. **d**, Schematic of Ceramidase activity assay. A fluorescently labelled C12-NBD-Ceramide was incubated for different time periods with varying concentrations of WT MBLAC2 or native cell lysates containing endogenously expressed ceramidases. The reaction was terminated by boiling and solvent evaporated. The reaction products were resuspended in $CHCl_3$/MeOH run on a TLC plate and developed with $CHCl_3$/MeOH/NH_4OH. Fluorescent substrates and products were read out at 488 nm. **e**, Ceramidase assay evaluation. Incubation of the fluorescently labelled ceramide with native cell lysates from MD-231 and HEK293 cells at 37 °C shows significant turnover of the substrate after 4 h of incubation and confirms the functional setup. **f**, Incubation of fluorescently labelled Ceramide with increasing concentration of MBLAC2 for 2h at 37 °C does not show significant turnover compared to negative control (−), while incubation with cell lysate reduces significantly the signal of intact ceramide substrate. **g**, Extended incubation of ceramide substrate with 1 μM WT MBLAC2 at 37 °C for increasing periods of time does not lead to significant substrate turnover even after 6 h incubation.

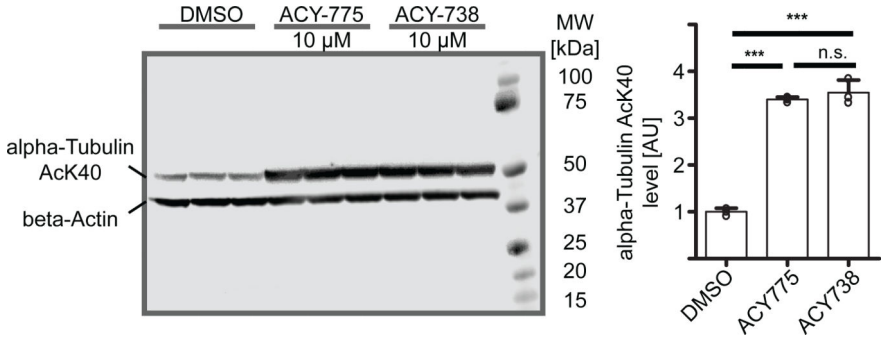

Extended Data Fig. 10. ACY-738 and ACY-775 induce similar HDAC6 substrate overacetylation. SW620 cells were treated for 6 h with ACY-738, ACY-775 or DMSO control and the lysates were used for western blots against acetylated alpha-Tubulin (Lys40). The intensities of analyte bands were normalized to beta-actin intensities of the same lane to control for loading amount biases. ACY-775 as well as ACY-738 induced significant overacetylation of alpha-Tubulin Lys40 (***: $p < 0.0001$, n.s: $p = 0.4147$). Similar overacetylation of

alpha-Tubulin indicates comparable target engagement of HDAC6 inhibitors. Data of bar chart are represented as mean +/− SD of three biological replicates (2-sided t-test).

Supplementary Material

Refer to Web version on PubMed Central for supplementary material.

Acknowledgements

The authors thank Wendy Greentree (Cornell) and Laura Wanat (TUM) for technical support. We gratefully acknowledge funding by the Deutsche Forschungsgemeinschaft (DFG) (SFB 1309, project 401883058 and project 407391208). M.I.P.M. and M.E.L. acknowledge support from the National Institutes of Health (grant GM121540). Contributions by V.W. and J.K.P. are funded by the Bavarian State Ministry of Science and the Arts within the framework of the Bavarian Research Institute for Digital Transformation (bidt). A.K.M. acknowledges the Helmholtz Drug Initiative for financial support. We also thank the CHDI foundation for generously providing CHDI00465983 and CHDI00390576.

References

1. Bettica P et al. Histological effects of givinostat in boys with Duchenne muscular dystrophy. Neuromuscul Disord 26, 643–649 (2016). [PubMed: 27566866]
2. Li Y & Seto E HDACs and HDAC Inhibitors in Cancer Development and Therapy. Cold Spring Harb Perspect Med 6 (2016).
3. Saito M et al. Acetylation of intrinsically disordered regions regulates phase separation. Nat Chem Biol 15, 51–61 (2019). [PubMed: 30531905]
4. Federspiel JD, Greco TM, Lum KK & Cristea IM Hdac4 Interactions in Huntington's Disease Viewed Through the Prism of Multiomics. Mol Cell Proteomics 18, S92–S113 (2019). [PubMed: 31040226]
5. Bardai FH & D'Mello SR Selective toxicity by HDAC3 in neurons: regulation by Akt and GSK3beta. J Neurosci 31, 1746–1751 (2011). [PubMed: 21289184]
6. Watson PJ et al. Insights into the activation mechanism of class I HDAC complexes by inositol phosphates. Nat Commun 7, 11262 (2016). [PubMed: 27109927]
7. Guenther MG, Barak O & Lazar MA The SMRT and N-CoR corepressors are activating cofactors for histone deacetylase 3. Mol Cell Biol 21, 6091–6101 (2001). [PubMed: 11509652]
8. Bantscheff M et al. Chemoproteomics profiling of HDAC inhibitors reveals selective targeting of HDAC complexes. Nat Biotechnol 29, 255–265 (2011). [PubMed: 21258344]
9. Becher I et al. Chemoproteomics reveals time-dependent binding of histone deacetylase inhibitors to endogenous repressor complexes. ACS Chem Biol 9, 1736–1746 (2014). [PubMed: 24877719]
10. Turnbull RE et al. The MiDAC histone deacetylase complex is essential for embryonic development and has a unique multivalent structure. Nat Commun 11, 3252 (2020). [PubMed: 32591534]
11. Weigt D, Hopf C & Medard G Studying epigenetic complexes and their inhibitors with the proteomics toolbox. Clin Epigenetics 8, 76 (2016). [PubMed: 27437033]
12. Asfaha Y et al. Recent advances in class IIa histone deacetylases research. Bioorg Med Chem 27, 115087 (2019). [PubMed: 31561937]
13. Millard CJ, Watson PJ, Fairall L & Schwabe JWR Targeting Class I Histone Deacetylases in a "Complex" Environment. Trends Pharmacol Sci 38, 363–377 (2017). [PubMed: 28139258]
14. Malgapo MIP, Safadi JM & Linder ME Metallo-beta-lactamase domain-containing protein 2 is S-palmitoylated and exhibits acyl-CoA hydrolase activity. J Biol Chem 296, 100106 (2020). [PubMed: 33219126]
15. Medard G et al. Optimized chemical proteomics assay for kinase inhibitor profiling. J Proteome Res 14, 1574–1586 (2015). [PubMed: 25660469]
16. Robers MB et al. Target engagement and drug residence time can be observed in living cells with BRET. Nat Commun 6, 10091 (2015). [PubMed: 26631872]

17. Bradner JE et al. Chemical phylogenetics of histone deacetylases. Nat Chem Biol 6, 238–243 (2010). [PubMed: 20139990]
18. Becher I et al. Thermal profiling reveals phenylalanine hydroxylase as an off-target of panobinostat. Nat Chem Biol 12, 908–910 (2016). [PubMed: 27669419]
19. Samaras P et al. ProteomicsDB: a multi-omics and multi-organism resource for life science research. Nucleic Acids Res 48, D1153–D1163 (2020). [PubMed: 31665479]
20. Heinzlmeir S et al. Chemoproteomics-Aided Medicinal Chemistry for the Discovery of EPHA2 Inhibitors. ChemMedChem 12, 999–1011 (2017). [PubMed: 28544567]
21. Balasubramanian S et al. A novel histone deacetylase 8 (HDAC8)-specific inhibitor PCI-34051 induces apoptosis in T-cell lymphomas. Leukemia 22, 1026–1034 (2008). [PubMed: 18256683]
22. Shen S et al. Structural and in Vivo Characterization of Tubastatin A, a Widely Used Histone Deacetylase 6 Inhibitor. ACS Med Chem Lett 11, 706–712 (2020). [PubMed: 32435374]
23. Geraldy M et al. Selective Inhibition of Histone Deacetylase 10: Hydrogen Bonding to the Gatekeeper Residue is Implicated. J Med Chem 62, 4426–4443 (2019). [PubMed: 30964290]
24. Buggy JJ et al. CRA-024781: a novel synthetic inhibitor of histone deacetylase enzymes with antitumor activity in vitro and in vivo. Mol Cancer Ther 5, 1309–1317 (2006). [PubMed: 16731764]
25. Heimburg T et al. Structure-Based Design and Synthesis of Novel Inhibitors Targeting HDAC8 from Schistosoma mansoni for the Treatment of Schistosomiasis. J Med Chem 59, 2423–2435 (2016). [PubMed: 26937828]
26. Bergman JA et al. Selective histone deacetylase 6 inhibitors bearing substituted urea linkers inhibit melanoma cell growth. J Med Chem 55, 9891–9899 (2012). [PubMed: 23009203]
27. Runkle KB et al. Inhibition of DHHC20-Mediated EGFR Palmitoylation Creates a Dependence on EGFR Signaling. Mol Cell 62, 385–396 (2016). [PubMed: 27153536]
28. Huttlin EL et al. Dual proteome-scale networks reveal cell-specific remodeling of the human interactome. Cell 184, 3022–3040 e3028 (2021). [PubMed: 33961781]
29. Kustatscher G et al. Co-regulation map of the human proteome enables identification of protein functions. Nat Biotechnol 37, 1361–1371 (2019). [PubMed: 31690884]
30. Chao OS et al. The HDAC6 Inhibitor Tubacin Induces Release of CD133(+) Extracellular Vesicles From Cancer Cells. J Cell Biochem 118, 4414–4424 (2017). [PubMed: 28452069]
31. Trajkovic K et al. Ceramide triggers budding of exosome vesicles into multivesicular endosomes. Science 319, 1244–1247 (2008). [PubMed: 18309083]
32. Lobera M et al. Selective class IIa histone deacetylase inhibition via a nonchelating zinc-binding group. Nat Chem Biol 9, 319–325 (2013). [PubMed: 23524983]
33. Burli RW et al. Design, synthesis, and biological evaluation of potent and selective class IIa histone deacetylase (HDAC) inhibitors as a potential therapy for Huntington's disease. J Med Chem 56, 9934–9954 (2013). [PubMed: 24261862]
34. Luckhurst CA et al. Potent, Selective, and CNS-Penetrant Tetrasubstituted Cyclopropane Class IIa Histone Deacetylase (HDAC) Inhibitors. ACS Med Chem Lett 7, 34–39 (2016). [PubMed: 26819662]
35. Hailu GS et al. Lysine Deacetylase Inhibitors in Parasites: Past, Present, and Future Perspectives. J Med Chem 60, 4780–4804 (2017). [PubMed: 28241112]
36. Lin A et al. Off-target toxicity is a common mechanism of action of cancer drugs undergoing clinical trials. Sci Transl Med 11 (2019).
37. Hai Y, Shinsky SA, Porter NJ & Christianson DW Histone deacetylase 10 structure and molecular function as a polyamine deacetylase. Nat Commun 8, 15368 (2017). [PubMed: 28516954]
38. Arrowsmith CH et al. The promise and peril of chemical probes. Nat Chem Biol 11, 536–541 (2015). [PubMed: 26196764]
39. Oehme I et al. Histone deacetylase 10 promotes autophagy-mediated cell survival. Proc Natl Acad Sci U S A 110, E2592–2601 (2013). [PubMed: 23801752]
40. Ridinger J et al. Dual role of HDAC10 in lysosomal exocytosis and DNA repair promotes neuroblastoma chemoresistance. Sci Rep 8, 10039 (2018). [PubMed: 29968769]

41. Fuller NO et al. CoREST Complex-Selective Histone Deacetylase Inhibitors Show Prosynaptic Effects and an Improved Safety Profile To Enable Treatment of Synaptopathies. ACS Chem Neurosci 10, 1729–1743 (2019). [PubMed: 30496686]
42. Mazitschek R & Payne N Resolving the Deceptive Isoform and Complex Selectivity of HDAC1/2 Inhibitors. Available at SSRN: https://ssrn.com/abstract=3960267 (2022).
43. Reinecke M et al. Chemoproteomic Selectivity Profiling of PIKK and PI3K Kinase Inhibitors. ACS Chem Biol 14, 655–664 (2019). [PubMed: 30901187]
44. Klaeger S et al. Chemical Proteomics Reveals Ferrochelatase as a Common Off-target of Kinase Inhibitors. ACS Chem Biol 11, 1245–1254 (2016). [PubMed: 26863403]
45. Gao B et al. Knockdown of ISOC1 inhibits the proliferation and migration and induces the apoptosis of colon cancer cells through the AKT/GSK-3beta pathway. Carcinogenesis 41, 1123–1133 (2020). [PubMed: 31740942]
46. Benoy V et al. Development of Improved HDAC6 Inhibitors as Pharmacological Therapy for Axonal Charcot-Marie-Tooth Disease. Neurotherapeutics 14, 417–428 (2017). [PubMed: 27957719]
47. Gold WA, Lacina TA, Cantrill LC & Christodoulou J MeCP2 deficiency is associated with reduced levels of tubulin acetylation and can be restored using HDAC6 inhibitors. J Mol Med (Berl) 93, 63–72 (2015). [PubMed: 25209898]
48. Benoy V et al. HDAC6 is a therapeutic target in mutant GARS-induced Charcot-Marie-Tooth disease. Brain 141, 673–687 (2018). [PubMed: 29415205]
49. Guo W et al. HDAC6 inhibition reverses axonal transport defects in motor neurons derived from FUS-ALS patients. Nat Commun 8, 861 (2017). [PubMed: 29021520]
50. Wang J et al. Functional analysis of the purified anandamide-generating phospholipase D as a member of the metallo-beta-lactamase family. J Biol Chem 281, 12325–12335 (2006). [PubMed: 16527816]
51. Cox J et al. Accurate proteome-wide label-free quantification by delayed normalization and maximal peptide ratio extraction, termed MaxLFQ. Mol Cell Proteomics 13, 2513–2526 (2014). [PubMed: 24942700]
52. Berg S et al. ilastik: interactive machine learning for (bio)image analysis. Nat Methods 16, 1226–1232 (2019). [PubMed: 31570887]
53. Steimbach RR et al. Aza-SAHA Derivatives are Selective Histone Deacetylase 10 Chemical Probes That Inhibit Polyamine Deacetylation. ChemRiv. (2021).
54. Jennings BC et al. 2-Bromopalmitate and 2-(2-hydroxy-5-nitro-benzylidene)-benzo[b]thiophen-3-one inhibit DHHC-mediated palmitoylation in vitro. J Lipid Res 50, 233–242 (2009). [PubMed: 18827284]
55. Okino N, Tani M, Imayama S & Ito M Purification and characterization of a novel ceramidase from Pseudomonas aeruginosa. J Biol Chem 273, 14368–14373 (1998). [PubMed: 9603946]
56. Tyanova S & Cox J Perseus: A Bioinformatics Platform for Integrative Analysis of Proteomics Data in Cancer Research. Methods Mol Biol 1711, 133–148 (2018). [PubMed: 29344888]
57. Johnson WE, Li C & Rabinovic A Adjusting batch effects in microarray expression data using empirical Bayes methods. Biostatistics 8, 118–127 (2007). [PubMed: 16632515]
58. Witting M, Maier TV, Garvis S & Schmitt-Kopplin P Optimizing a ultrahigh pressure liquid chromatography-time of flight-mass spectrometry approach using a novel sub-2mum core-shell particle for in depth lipidomic profiling of Caenorhabditis elegans. J Chromatogr A 1359, 91–99 (2014). [PubMed: 25074420]
59. Tsugawa H et al. A lipidome atlas in MS-DIAL 4. Nat Biotechnol 38, 1159–1163 (2020). [PubMed: 32541957]
60. Dieterle F, Ross A, Schlotterbeck G & Senn H Probabilistic quotient normalization as robust method to account for dilution of complex biological mixtures. Application in 1H NMR metabonomics. Anal Chem 78, 4281–4290 (2006). [PubMed: 16808434]

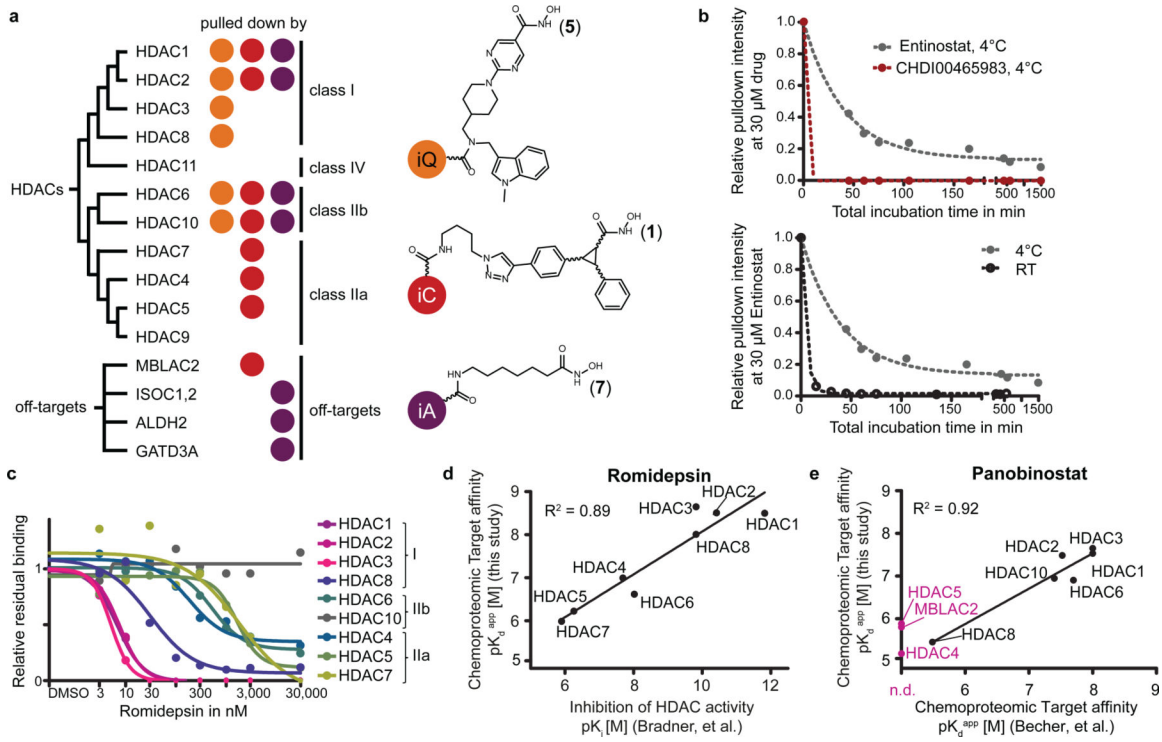

Fig. 1 |. Chemical proteomics assay for HDAC inhibitors.

a, Contribution of each of the three selected affinity probes to the enrichment of Zn-HDACs and off-targets from mixed SW620 and MV4–11 cell lysates. **b**, Temperature-dependence of aminoanilide (Entinostat) and hydroxamate (CHDI00465983) drugs on target engagement over a time course of up to 25 h. When binding equilibrium is reached, maximal occupancy of the target binding sites is obtained and minimal enrichment by the affinity matrix ensues (minimal residual binding is synonymous with maximal competition). **c**, Exemplary dose-response curves for Romidepsin binding to HDACs using the optimized chemical proteomics assay. **d**, Correlation analysis between apparent dissociation constants (pK_d^{app}, p denotes −log10) of Romidepsin: HDAC interactions determined by the chemical proteomics assay and published pK_i values (−log10 of inhibitory constant) obtained by *in vitro* recombinant enzyme activity assays[17]. **e**, Correlation analysis between apparent dissociation constants (pK_d^{app}) of Panobinostat: HDAC interactions determined by the chemical proteomics assay and previously published chemical proteomics profiling[18]. Additional targets covered in this study (class IIa HDAC4/5 and MBLAC2) are marked in purple.

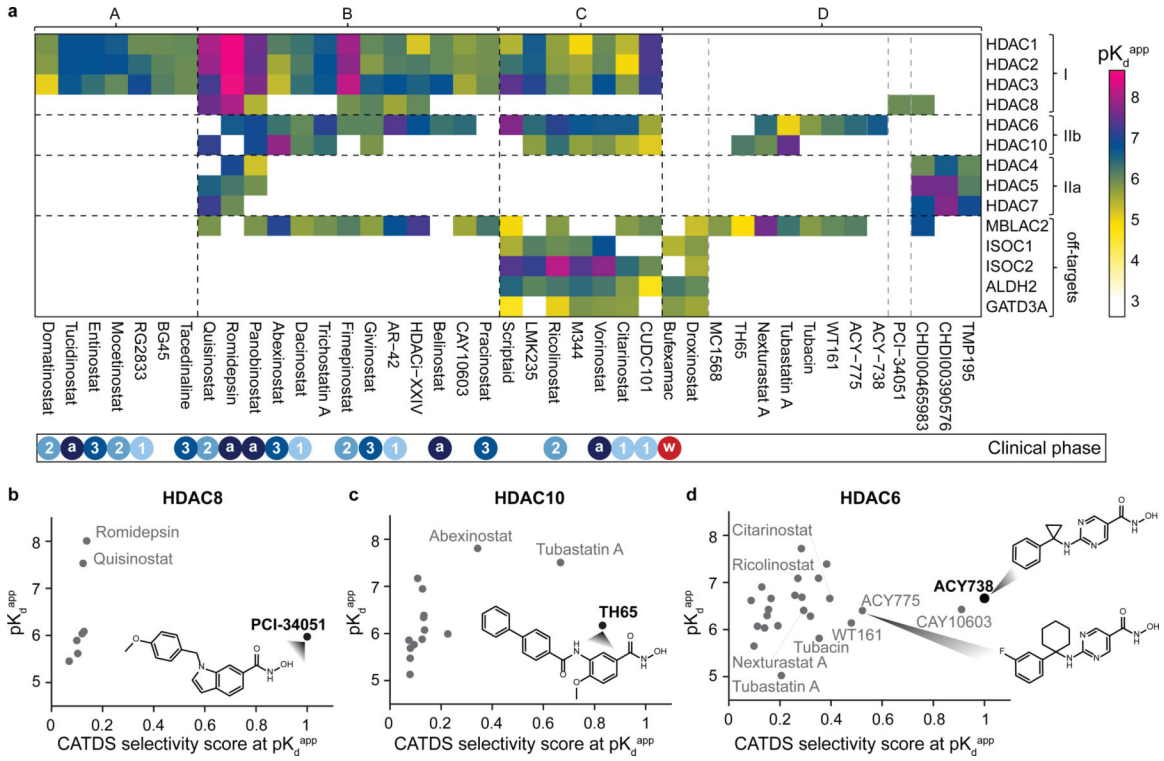

Fig. 2 |. Target landscape of HDAC and metallohydrolase drugs.

a, Heatmap of pK_d^{app} values obtained for 41 drugs and 14 targets using the presented chemical proteomics competition assay. A – D denotes groups of drugs that share similar target profiles. Coloured circles at the bottom of the panel indicate the clinical status of each drug: 'a' is approved, 'w' withdrawn and '1–3' phase of clinical development (1–3) (https://clue.io/repurposing-app). **b-d**, Scatter plots displaying the affinity of drugs binding to HDAC8, HDAC10 or HDAC6 (pK_d^{app}) against their selectivity as measured by CATDS[20] (concentration- and target-dependent selectivity; calculated for the respective target HDAC at its pK_d^{app}, also see Supplementary Fig. 3 and text for details). The most selective compounds for a given target are marked by arrowheads and shown in bold. Structures for the most selective drugs are shown, as well as for the less-selective drug ACY-775 because of its chemical similarity to ACY-738 that we later exploit to probe MBLAC2 (see below).

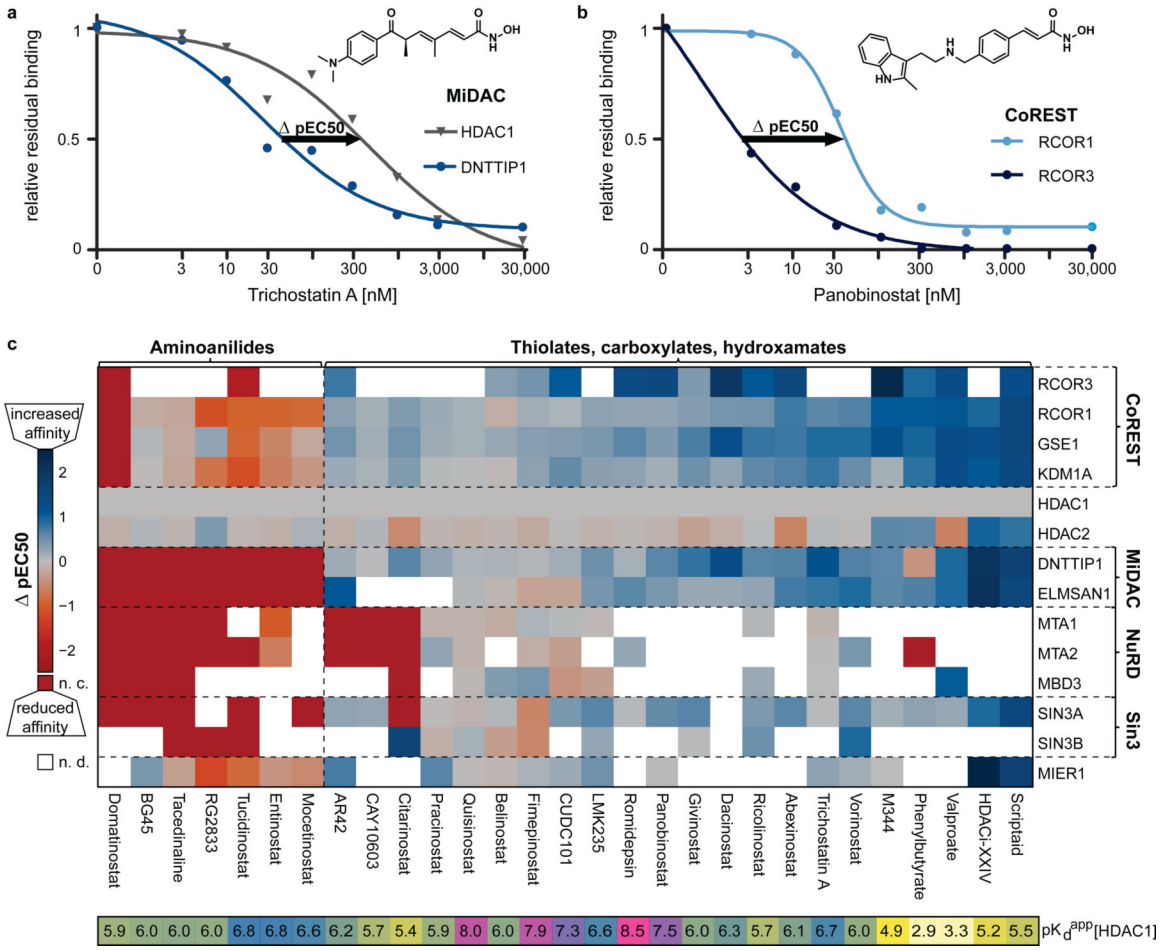

Fig. 3 |. Complex selectivity of class I HDACis.

a, Dose-response binding curves for Trichostatin A versus HDAC1 and DNTTIP1 (representing the MiDAC complex). The difference between the two inflection points of dose response curves is marked by ΔpEC_{50} (pEC_{50} is $-\log10EC_{50}$). **b**, same as panel a but for Panobinostat and the CoREST subunits RCOR1 and RCOR3. **c**, Heatmap showing ΔpEC_{50} ($pEC_{50}^{Interactor}$-pEC_{50}^{HDAC1}) values for class I HDAC inhibitors and HDAC complex proteins. n. d. denotes that no value was determined. The bar at the bottom lists HDAC1 pK_d^{app} values of the corresponding HDAC inhibitor.

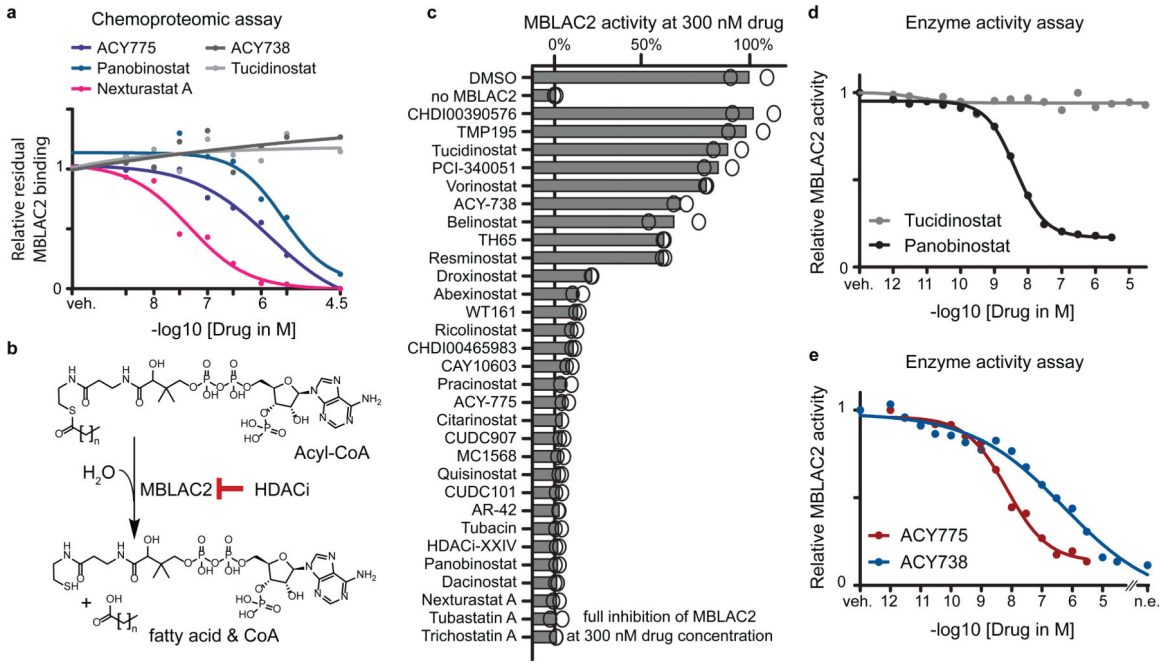

Fig. 4 |. HDAC inhibitors abrogate MBLAC2 acyl-CoA hydrolase activity at nanomolar concentrations.

a, Chemoproteomic dose-response binding curve of MBLAC2 and five HDACis (veh. = vehicle control). **b**, Reaction scheme of MBLAC2-catalyzed hydrolysis of acyl-CoA. **c**, Bar plot summarizing results of a single dose MBLAC2 enzyme inhibition screen using HDACis. Bars represent the relative rate of [^{3}H]-palmitoyl-CoA hydrolysis in the presence of recombinant MBLAC2 (30 nM) and 24 HDACis at 300 nM drug concentration (mean of two measurements, whiskers of error bar denote the standard deviation). **d**, Dose-dependent inhibition of MBLAC2 activity by approved HDACis. pEC_{50} denotes –log10 effective concentration). **e**, same as panel ‘d’ but for two structurally related compounds (n.e.= no enzyme, veh. = vehicle control).

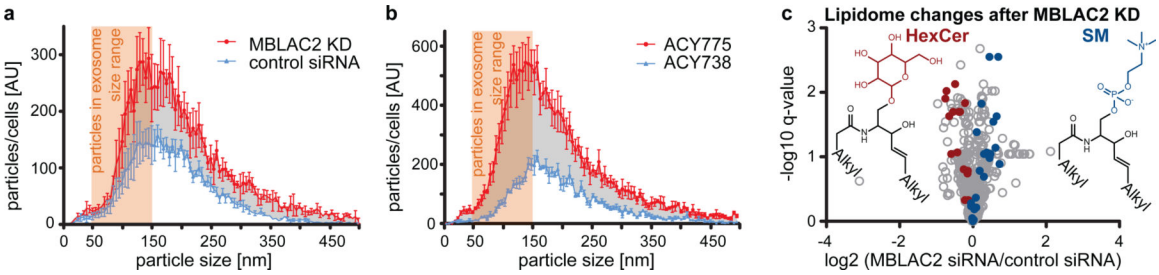

Fig. 5 |. MBLAC2 knockdown or inhibition lead to vesicle accumulation in supernatants of HEK293 cells.

a, Number and size distribution of extracellular vesicles isolated from HEK293 cell supernatants following MBLAC2 knockdown by siRNA pools (n=3 biological replicates, data are shown as mean +/− SEM). The orange area marks the typical size range of exosomes. **b**, same as panel 'a' but for the dual HDAC6/MBLAC2 inhibitor ACY-775 (3 μM) and the selective HDAC6 inhibitor ACY-738 (3 μM) (n=3 biological replicates, data are shown as mean +/− SEM). **c**, volcano plot summarizing the response of the lipidome of HEK293 cells in response to MBLAC2 knockdown (n=3 experiments). Members of the hexosylceramide (HexCer) and sphingomyeline (SM) families are highlighted and their generic structures are shown.